Research Square

Preprints are preliminary reports that have not undergone peer review.
They should not be considered conclusive, used to inform clinical practice,
or referenced by the media as validated information.

Copper-Based Targeted Nanozyme Platform with Sequential Phototherapy-Enzymatic Therapy for Orchestrating Macrophage Homeostasis in Rheumatoid Arthritis

Zeyu Han
Shanghai Ninth People's Hospital
Zhan Liu
Shanghai Ninth People's Hospital
Shoufu Sun
Tongren Hospital
Rui Chao
Shanghai Ninth People's Hospital
Xinao Fan
Shanghai Ninth People's Hospital
Xuzhuo Chen
Shanghai Ninth People's Hospital
Fan Li
Affiliated Hospital of Qingdao University
Shanyong Zhang
ZHANGSY1787@sh9hospital.org.cn

Shanghai Ninth People's Hospital

Research Article

Keywords: Rheumatoid arthritis, Nanozyme, Sequential therapy, Photodynamic therapy, Macrophage polarization

Posted Date: July 27th, 2026

DOI: https://doi.org/10.21203/rs.3.rs-10346257/v1

License: This work is licensed under a Creative Commons Attribution 4.0 International License.
Read Full License

Additional Declarations: No competing interests reported.

Version of Record: A version of this preprint was published at Journal of Nanobiotechnology on October 7th, 2026. See the published version at https://doi.org/10.1186/s12951-026-05136-0.

Copper-Based Targeted Nanozyme Platform with Sequential Phototherapy-Enzymatic Therapy for Orchestrating Macrophage Homeostasis in Rheumatoid Arthritis

Zeyu Han[#a], *Zhan Liu*[#a], *Shoufu Sun*[#b], *Rui Chao*[a], *Xinao Fan*[a], *Xuzhuo Chen*[a*], *Fan Li*[cd*] *and Shanyong Zhang*[a*]

[a] Department of Oral Surgery, Shanghai Ninth People's Hospital, Shanghai Jiao Tong University School of Medicine; College of Stomatology, Shanghai Jiao Tong University; National Center for Stomatology; National Clinical Research Center for Oral Diseases; Shanghai Key Laboratory of Stomatology; Shanghai Research Institute of Stomatology, Shanghai, 200011, China.

[b] Tongren Hospital, Shanghai Jiao Tong University School of Medicine, Shanghai 200336, China.

[c] Department of Oral Implantology, The Affiliated Hospital of Qingdao University, Qingdao University, Qingdao, 266000, China.

[d] School of Stomatology, Qingdao University, Qingdao, 266000, China

[#] These authors contributed equally to this work.

* Corresponding authors:

Xuzhuo Chen, E-mail: 822015@sh9hospital.org.cn

Fan Li, E-mail: lifan911017@qdu.edu.cn

Shanyong Zhang, E-mail: ZHANGSY1787@sh9hospital.org.cn

Abstract

Rheumatoid arthritis (RA) remains a formidable clinical challenge due to the vicious cycle of hyperactivated M1 macrophages, excessive reactive oxygen species (ROS), and sustained pro-inflammatory cytokine storm. Herein, we rationally engineer a targeted copper-based nanozyme platform (CPPF NPs) with sequential dual-wavelength phototherapy-enzymatic activities for spatiotemporally controlled macrophage homeostasis regulation in RA treatment. The CPPF NPs are fabricated via a stepwise surface engineering strategy, consisting of a copper-based nanozyme core with intrinsic superoxide dismutase (SOD)- and catalase (CAT)-like cascade activities, a polydopamine (PDA) photothermal conversion layer, a porphyrin (Por) photosensitizer, and a folic acid (FA) targeting ligand. Via FA-mediated active targeting toward M1 macrophages overexpressing folate receptors, CPPF NPs selectively accumulate in inflamed joints. Upon sequential laser irradiation, CPPF NPs first exert photodynamic therapy (PDT, 660 nm) to trigger rapid apoptosis of pro-inflammatory M1 macrophages, cutting off the source of inflammation at an early stage. Subsequently, mild photothermal therapy (PTT, 808 nm) cooperates with the inherent antioxidant nanozyme activity to scavenge residual ROS, upregulate heat shock protein 70 (HSP70) expression, and redirect residual macrophages toward the anti-inflammatory M2 phenotype. Such an "apoptosis induction–immune remodeling" sequential strategy effectively breaks the vicious cycle of oxidative stress and inflammation, thereby comprehensively remodeling the RA microenvironment. This work presents an integrated and biosafe nanotherapeutic strategy for precise and sequential treatment of RA, offering a promising paradigm for the intervention of other inflammation-related diseases.

Key words: Rheumatoid arthritis, Nanozyme, Sequential therapy, Photodynamic therapy, Macrophage polarization

Background

Rheumatoid arthritis (RA) is a chronic, systemic autoimmune disease characterized by persistent synovial inflammation, progressive cartilage destruction, and bone erosion, affecting approximately 1% of the global population [1, 2]. Despite significant advances in therapeutic strategies, including non-steroidal anti-inflammatory drugs (NSAIDs), disease-modifying antirheumatic drugs (DMARDs), and biological agents, the clinical management of RA remains challenging. Conventional treatments often suffer from systemic side effects, drug resistance, and inability to achieve long-term remission, highlighting the urgent need for novel, targeted, and multifunctional therapeutic approaches [3, 4].

The pathogenesis of RA is driven by a complex interplay between immune dysregulation and tissue destruction, with macrophage polarization imbalance playing a significant role [5-7]. In healthy joints, macrophages maintain a homeostatic balance between pro-inflammatory M1 and anti-inflammatory M2 phenotypes. However, in RA, the synovial microenvironment is dominated by hyperactivated M1 macrophages, which secrete excessive reactive oxygen species (ROS) and pro-inflammatory cytokines such as tumor necrosis factor-α (TNF-α), interleukin-1β (IL-1β), and interleukin-6 (IL-6) [8, 9]. These mediators not only directly induce chondrocyte apoptosis and extracellular matrix degradation but also recruit and activate additional immune cells, creating a self-sustaining vicious cycle of oxidative stress and inflammation [10, 11]. Crucially, persistent inflammation severely impairs microvasculature, creating a highly hypoxic microenvironment that further exacerbates M1 polarization and ROS accumulation [12-14]. Accumulating evidence indicates that disrupting this pathological cycle by selectively eliminating pathogenic M1 macrophages and restoring macrophage homeostasis represents a promising therapeutic strategy for RA [15-17].

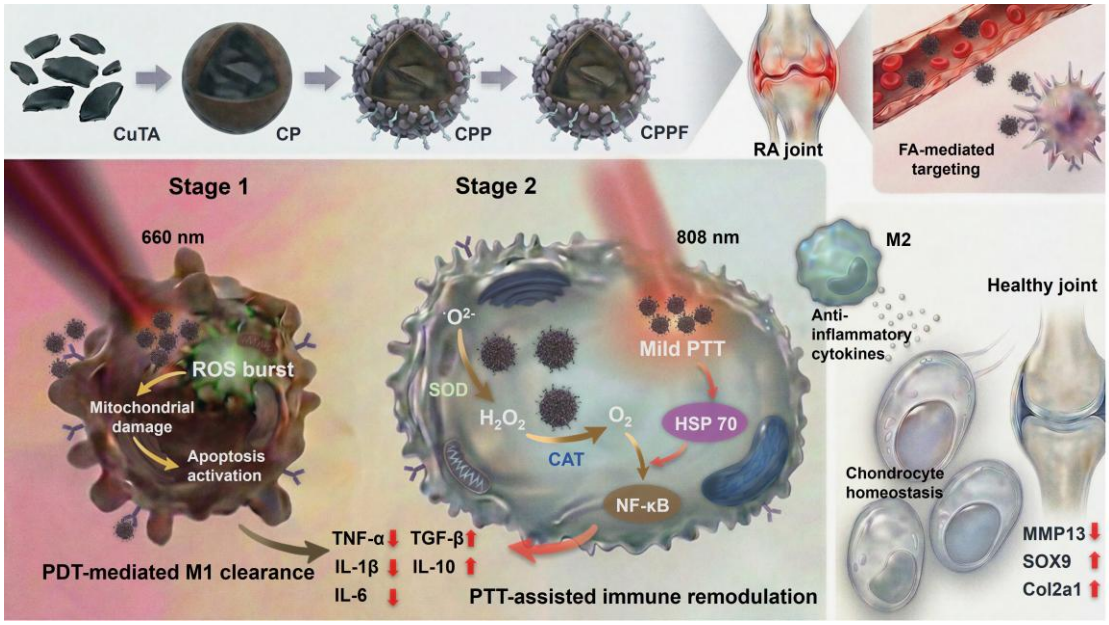
In recent years, phototherapies including photodynamic therapy (PDT) and

photothermal therapy (PTT) have emerged as attractive alternatives for RA treatment due to their non-invasiveness, spatiotemporal controllability, and low systemic toxicity [18-20]. PDT utilizes photosensitizers to generate cytotoxic ROS under specific wavelength irradiation, effectively inducing apoptosis in rapidly proliferating inflammatory cells [20-22]. However, conventional PDT often lacks sustained regulation of the residual oxidative stress after cell clearance, which may reactivate inflammatory pathways. On the other hand, mild PTT (42–46 ℃) has been shown to exert immunomodulatory effects by upregulating heat shock protein 70 (HSP70), which inhibits NF-κB signaling and promotes M2 macrophage polarization [23-26]. Nevertheless, mild PTT alone is insufficient to rapidly eliminate the large population of pathogenic M1 macrophages that serve as the primary source of inflammation [27, 28]. Therefore, integrating PDT and PTT with complementary mechanisms could potentially achieve superior therapeutic outcomes by combining rapid cell killing with long-term immune remodeling [29].

Nanozymes, functional nanomaterials with intrinsic enzyme-mimetic activities, have revolutionized the field of inflammatory disease therapy by providing a robust platform for simultaneous ROS scavenging and immune regulation [30-32]. Among various nanozymes, copper-based nanozymes have attracted particular attention due to their excellent biocompatibility, facile synthesis, and cascade catalytic activities resembling superoxide dismutase (SOD) and catalase (CAT) [33, 34]. These activities enable copper-based nanozymes to efficiently convert toxic superoxide anions ($^{\bullet}O_2^-$) and hydrogen peroxide (H_2O_2) into harmless water and oxygen, thereby alleviating oxidative stress and hypoxia in the inflammatory microenvironment [33, 35]. However, the therapeutic efficacy of unmodified copper-based nanozymes is limited by their poor aqueous solubility and lack of targeting capability, leading to non-specific distribution and reduced accumulation at inflamed joints.

To address these challenges, we herein report a rationally designed targeted nanozyme platform, CuTA@PDA-Por/FA (CPPF NPs), for sequential phototherapy-enzymatic synergistic therapy of RA. The CPPF NPs were constructed via a stepwise surface

engineering strategy: a copper tannic acid coordination (CuTA) nanozyme core with cascade catalytic activity was coated with a polydopamine (PDA) shell, which was further functionalized with the photosensitizer porphyrin (Por) and the targeting ligand folic acid (FA). Specifically, the design rationale of CPPF NPs follows a biologically dictated "clearance first, remodeling later" sequential therapeutic logic: folic acid-mediated active targeting enables specific accumulation of CPPF NPs in activated M1 macrophages that overexpress folate receptor [20, 36]; the CAT-like activity of the CuTA core generates oxygen to alleviate hypoxia, thereby potentiating Por-mediated PDT effects to induce rapid apoptosis of M1 macrophages upon 660 nm laser irradiation, immediately blocking the main source of pro-inflammatory mediators; subsequent 808 nm laser irradiation elicits mild PTT from the PDA shell, which synergizes with the intrinsic SOD/CAT activities of the CuTA core to scavenge residual ROS, upregulate HSP70 expression, and drive macrophage polarization toward the anti-inflammatory M2 phenotype. This integrated strategy effectively breaks the vicious cycle of oxidative stress and inflammation, leading to comprehensive remodeling of the RA microenvironment. This work not only provides a novel multifunctional nanozyme platform for RA treatment but also offers a generalizable strategy for the management of other inflammatory diseases characterized by macrophage dysregulation.



Scheme 1. Synthesis of CPPF NPs, and illustration of sequential phototherapy-

enzymatic therapy for orchestrating macrophage homeostasis in RA.

Materials and methods

Materials

Copper sulfate pentahydrate, tannic acid (TA), dopamine hydrochloride, tris(hydroxymethyl)aminomethane (Tris) buffer, 1-ethyl-3-(3-dimethylaminopropyl)carbodiimide hydrochloride (EDC), N-hydroxysuccinimide (NHS), 1,3-diphenylisobenzofuran (DPBF) and hydrogen peroxide (H_2O_2) were purchased from Aladdin Biochemical Technology Co., Ltd. 5-(4-Carboxyphenyl)-10,15,20-triphenylporphyrin (Por-COOH) was acquired from Zhengzhou Alfa Chemical Co., Ltd., while thiolated polyethylene glycol-folic acid (SH-PEG-FA) was supplied by Ruixi Biological Technology Co., Ltd. PE-conjugated anti-mouse CD86 and FITC-conjugated anti-mouse CD206 antibodies were obtained from Elabscience Biotechnology. Cell Counting Kit-8 (CCK-8), 2',7'-dichlorofluorescein diacetate (DCFH-DA), Annexin V-FITC/PI apoptosis detection kit, ABTS total antioxidant capacity assay kit, SOD assay kit (WST-8 method) and catalase assay kit were all procured from Beyotime Biotechnology.

Synthesis of CuTA@PDA-Por/FA (CPPF) NPs

CuTA were fabricated through a straightforward metal-ligand coordination reaction between copper ions and TA. In a typical procedure, 81 mg of TA and 2625 mg of copper sulfate pentahydrate were individually dissolved in deionized water, and the two solutions were mixed and diluted to a total volume of 150 mL. The pH of the mixture was adjusted to 7.4 by dropwise addition of approximately 7 mL of 2 M sodium hydroxide solution. The reaction system was then placed in a 60 ℃ preheated oil bath and stirred continuously for 5 hours. The obtained brown precipitate was harvested by centrifugation at 6000 rpm for 3 minutes, washed three times with deionized water and once with absolute ethanol, and dried under vacuum at 60 ℃ for 1 hour. The purified CuTA were stored at 4 ℃ for subsequent experiments.

The multifunctional CPPF NPs were synthesized via a stepwise surface

functionalization strategy. Briefly, 50 mg of CuTA powder was dispersed in 50 mL Tris buffer (pH 8.5) by ultrasonication for 15 min, followed by the addition of 50 mg dopamine hydrochloride. The in situ polymerization reaction proceeded at room temperature to form CuTA@PDA (CP) NPs, which were collected by centrifugation at 12,000 rpm for 10 min, washed three times with deionized water, and lyophilized. Subsequently, 2.5 mg Por-COOH was dissolved in 20 mL deionized water and activated with 6.80 mg EDC and 2.05 mg NHS for 30 min at room temperature under a nitrogen atmosphere. 50 mg of CP NPs dispersed in 20 mL deionized water were then added, and the amide condensation reaction continued for 24 h in the dark. The resulting CuTA@PDA-Por (CPP) NPs were purified by centrifugation and lyophilization. Finally, 50 mg of CPP NPs were dispersed in 40 mL deionized water by ultrasonication, and 20 mg of SH-PEG-FA were added. The Michael addition reaction proceeded at room temperature for 12 h in the dark under nitrogen atmosphere. The final CPPF NPs were also collected by centrifugation and lyophilization.

Characterization

The morphology and structure of the nanoparticles were observed by transmission electron microscopy (TEM, JEM2010, Japan). The hydrated particle size distribution and zeta potential were determined by dynamic light scattering (DLS, Nano ZS90, UK). The UV-visible absorption spectra were recorded using a UV-vis spectrophotometer (PerkinElmer LAMBDA 950, USA). Fourier transform infrared spectra were obtained via a Fourier transform infrared spectrometer (FTIR, Nicolet 5700, USA). The crystal structures of the samples were confirmed by X-ray diffraction (XRD, Bruker D8 Advance, Germany). Raman spectra were recorded on a Raman microscope (Renishaw inVia, UK) with a 785 nm laser excitation source. The elemental composition and chemical valence states were analyzed by X-ray photoelectron spectroscopy (XPS, Thermo Fisher Scientific, USA). The specific surface area and pore structure parameters were derived from N_2 adsorption-desorption isotherms using a Brunauer-Emmett-Teller surface area analyzer (BET, Kubo X1000, China).

Por loading content and entrapment efficiency determination

The Por loading content and entrapment efficiency were determined by measuring the concentration of unbound free Por in the supernatant after CPP synthesis. The absorbance of the supernatant at 575 nm was measured using a UV-vis spectrophotometer, and the concentration of free Por was calculated based on a pre-established Por standard curve. The Por loading content and entrapment efficiency were calculated according to the following equations:

Loading content (%) = (Amount of loaded Por / Amount of CPP NPs) × 100%

Entrapment efficiency (%) = (Amount of loaded Por / Amount of initial Por) × 100%

PDT and PTT performance evaluation

DPBF was used as a chemical probe to detect the generation of singlet oxygen. In a typical experiment, DPBF was added to CPPF solutions to record the absorbance intensity at 420 nm. The absorbance was measured every 30 seconds during 660 nm laser irradiation. A DPBF solution without CPPF NPs was used as the control.

CPPF NPs solutions with different concentrations (0-400 μg/mL) were irradiated with an 808 nm laser for 10 min, and the temperature was recorded every 30 s using a digital thermometer. Infrared thermal images were captured at different time points using a thermal camera. The PTT stability of CPPF NPs was evaluated through four consecutive heating-cooling cycles. Briefly, 3 mL of CPPF NPs solution was irradiated with an 808 nm laser for 10 min, then allowed to cool to room temperature naturally. This cycle was repeated four times, and the temperature change was recorded in each cycle. To evaluate the long-term PTT stability, the same experiment was repeated with 1-day intervals between cycles.

Antioxidant and enzyme-mimetic activity assays

To comprehensively evaluate the antioxidant capacity and enzyme mimetic activity of CPPF NPs, ABTS radical scavenging assay, WST-8-based SOD-like activity assay, and catalase-like activity assay were performed according to the instructions. Different concentrations of CPPF NPs were first prepared to investigate the dose-dependent

antioxidant and enzymatic effects. Subsequently, the antioxidant and enzymatic activities of CuTA, CPPF, and laser-pretreated CPPF (CPPF+L, pre-irradiated with 660 nm laser for 3 min) were compared under identical experimental conditions to assess the impact of surface modification and short-term PDT on nanozyme performance.

CV measurements were performed on a CHI 660E electrochemical workstation using a standard three-electrode system. A glassy carbon electrode modified with CPPF NPs served as the working electrode, a 1 cm^2 platinum sheet as the counter electrode, and a saturated calomel electrode as the reference electrode. All measurements were conducted in 25 mL of 0.1 M tetrabutylammonium hexafluorophosphate in dichloromethane solution. The potential was scanned from -2.24 V to +2.24 V vs. SCE at a scan rate of 100 mV/s. A blank CV scan of the pure electrolyte solution was recorded prior to sample measurements.

Intracellular ROS scavenging assay

Intracellular ROS levels were detected using the DCFH-DA fluorescent probe. Briefly, RAW 264.7 cells were seeded in confocal microscopy dishes (35 mm) at a density of 1 × 10^5 cells per dish and allowed to adhere overnight, cells were then stimulated with 1 μg/mL LPS for 24 h. Subsequently, LPS-treated cells were incubated with CPPF NPs at concentrations of 50 μg/mL or 100 μg/mL for another 24 h. For the laser-pretreated group, CPPF NPs at 100 μg/mL were pre-irradiated with a 660 nm laser for 3 min and incubated at room temperature for 30 min before being added to the cells. After incubation, cells were washed three times with PBS, and stained with DCFH-DA at 37 ℃ for 20 min in the dark. Following three additional washes with PBS, cell nuclei were counterstained with Hoechst 33342 and visualized by CLSM.

Cytotoxicity assay

The cytotoxicity of CPPF NPs was evaluated using the CCK-8 assay. RAW 264.7 macrophages or ATDC5 chondrocytes were seeded in 96-well plates at a density of 5 × 10^3 cells/well and cultured overnight. The culture medium was then replaced with fresh medium containing different concentrations of CPPF NPs (0-200 μg/mL). After

incubation for 24 h, CCK-8 solution was added to each well, and the plates were incubated at 37 ℃ for 3 h. The absorbance at 450 nm was measured using a microplate reader.

Hemolysis assay

Fresh mouse blood was collected into EDTA-anticoagulant tubes and centrifuged at 1500 rpm for 10 minutes to isolate red blood cells (RBCs). The obtained RBCs were washed three times with PBS and resuspended to prepare a 10% RBC suspension. Subsequently, equal volumes of the RBC suspension were mixed with CPPF solutions at various concentrations. PBS and deionized water were employed as the negative and positive controls, respectively. After incubation at 37 ℃ for 2 hours, all samples were centrifuged, and the absorbance of the supernatants at 540 nm was determined using a microplate spectrophotometer.

In vitro cellular uptake assay

RAW 264.7 macrophages were seeded in confocal microscopy dishes and stimulated with 1 μg/mL LPS for 24 h after adhesion. The culture medium was then replaced with fresh medium containing CPPF NPs, and the cells were incubated for different time intervals (2, 4, 6, 8 h). At each time point, the cells were washed with PBS, fixed with 4% paraformaldehyde for 10 min, and stained with DAPI for 5 min to label the nuclei. The cellular uptake of CPPF NPs was finally observed by CLSM. For quantitative analysis by flow cytometry, cells were seeded, stimulated, and incubated with CPPF NPs under the same conditions as described above. At each designated time point, cells were harvested, washed and analyzed by flow cytometry.

To verify the FA-mediated targeting ability of CPPF NPs, flow cytometry analysis was performed. RAW 264.7 macrophages were seeded in 6-well plates and stimulated with 1 μg/mL LPS for 24 h. Then they were divided into 4 groups: Control group, CPP group, CPPF group, and FA blocking group (pre-incubated with 1 mM free FA for 1 h to block cell surface folate receptors). After incubation, the cells were harvested and analyzed using a flow cytometer. In addition, the phenotype-dependent cellular uptake of CPPF

NPs was also evaluated by flow cytometry. RAW 264.7 macrophages were seeded in 6-well plates at a density and polarized to different phenotypes: M0 (untreated), M1 (stimulated with 1 μg/mL LPS for 24 h), and M2 (stimulated with 50 ng/mL IL-4 for 12 h) [20]. Subsequently, the cells were incubated with CPPF for 6 h. After incubation, the cells were harvested and analyzed.

Intracellular PTT and PDT effects

The intracellular PTT of CPPF NPs in different macrophage phenotypes was evaluated using an infrared thermal imager and thermometer. RAW 264.7 macrophages were seeded in 6-well plates at a density of 1×10^5 cells/well, stimulated and divided into three groups: Control, M0, and M1. The culture medium was replaced with fresh medium containing CPPF NPs for the M0 and M1 groups, while the Control group was incubated with an equal volume of PBS. After 6 h of incubation, all cells were washed three times with PBS and irradiated with an 808 nm laser for 5 min. The temperature changes and infrared thermal images were recorded every 1 min during laser irradiation.

The cytotoxicity of CPPF NPs-mediated PDT against pro-inflammatory M1 macrophages was assessed by CCK-8 assay. M1-polarized RAW 264.7 macrophages were seeded in 96-well plates at a density of 5×10^3 cells/well and incubated for 24 h. The cells were incubated with different concentrations of CPPF NPs for 6 h, then washed with PBS and irradiated with a 660 nm laser for 3 min. After an additional 24 h incubation, CCK-8 reagent was added to each well, and the plates were further incubated at 37 ℃ for 3 h before measuring the absorbance at 450 nm.

Subsequently, to further clarify the mechanism of cell death induced by CPPF NPs-based sequential phototherapy, Annexin V-FITC/PI staining was performed to quantify apoptotic cell populations. RAW 264.7 macrophages were seeded in 6-well plates and M1-polarized, the cells were then divided into five groups: Control (untreated); Laser (irradiated with 660 nm laser for 3 min followed by 808 nm laser for 15 min); NPs (incubated with CPPF NPs for 6 h); (4) NPs+660 nm (incubated with CPPF NPs for 6 h, then irradiated with 660 nm laser for 3 min); (5) NPs+660/808 nm (incubated with

CPPF NPs for 6 h, then irradiated with 660 nm laser for 3 min followed by 808 nm laser for 15 min). After treatment, the cells were incubated for another 6 h, collected, and stained with Annexin V-FITC and PI according to the manufacturer's instructions. The apoptotic cell population was analyzed by flow cytometry.

Macrophage polarization assay

RAW 264.7 macrophages were seeded in 6-well plates at a density of 2×10^5 cells/well and incubated for 24 h. The cells were stimulated with 1 μg/mL LPS for 24 h to induce M1 polarization, and then divided into five groups: Control group, Laser group, NPs group, NPs+660 nm group, and NPs+660/808 nm group. Importantly, all cells were treated for a total of 3 days: 660 nm laser irradiation was performed only on day 1 for 3 min, while 808 nm laser irradiation was applied daily for 15 min.

For immunofluorescence staining, the cells were fixed with 4% paraformaldehyde for 10 min, permeabilized with 0.2% Triton X-100 for 10 min, and blocked with blocking goat serum for 1 h at 37 ℃. The cells were then incubated with primary antibodies against iNOS (1:500) and CD206 (1:500) overnight at 4 ℃, followed by incubation with Alexa Fluor 594-conjugated secondary antibodies (1:1000) for 1 h at room temperature. The nuclei were stained with DAPI for 5 min, and the cells were observed by CLSM.

For flow cytometry analysis, the cells were collected, washed with PBS, and stained with PE-conjugated anti-mouse CD86 and FITC-conjugated anti-mouse CD206 for 30 min at 4 ℃ in the dark. The stained cells were analyzed by flow cytometry.

For Western blot analysis, the cells were lysed with RIPA lysis buffer containing protease inhibitors. The protein concentration was determined using the BCA protein assay kit. Equal amounts of protein were separated by SDS-PAGE and transferred to PVDF membranes. The membranes were blocked with 5% skim milk for 2 h at room temperature, then incubated with primary antibodies against iNOS (1:1000), HSP70 (1:1000), and GAPDH (1:5000) overnight at 4 ℃. After washing three times with TBST, the membranes were incubated with HRP-conjugated secondary antibodies (1:5000)

for 1 h at room temperature. The protein bands were visualized using an enhanced chemiluminescence reagent, and the band intensities were quantified using ImageJ software.

For ELISA analysis, the cell culture supernatants were collected, and the concentrations of TNF-α, IL-1β, IL-6, IL-10, and TGF-β were measured using commercial ELISA kits according to the manufacturers' instructions.

Transcriptomic analysis

LPS-induced M1 macrophages were divided into three groups: (1) Control (LPS only); (2) NPs (LPS + CPPF NPs); (3) NPs+L (LPS + CPPF NPs + 660 nm laser irradiation for 3 min). After treatment, the cells were incubated for another 24 h. Total RNA was extracted using Trizol reagent. For functional analysis, GO and KEGG pathway enrichment analyses were conducted utilizing Hiplot Cloud (https://hiplot.com.cn/).

Transwell co-culture experiment

Transwell co-culture experiments were performed using 24-well Transwell inserts. RAW 264.7 macrophages were seeded in the upper chamber at a density of 5×10^3 cells/well and stimulated with 1 μg/mL LPS for 24 h to induce M1 polarization. The macrophages were then treated with different regimens as described in section 4.12. Meanwhile, ATDC5 chondrocytes or BMSCs were seeded in another 24-well plate at a density of 1×10^4 cells/well. After different treatment, the upper chamber containing RAW 264.7 was transferred to the lower chamber containing chondrocytes or BMSCs, and the cells were co-cultured for 48 h. After co-culture, the viability of ATDC5 chondrocytes and BMSCs in the lower chamber was measured using the CCK-8 assay. The protein expression of MMP13, Col2a1, and Sox9 in ATDC5 cells was detected by Western blot analysis. The concentrations of TNF-α, IL-1β, and IL-10 in the co-culture supernatant were measured by ELISA.

Establishment of CIA mouse model

All animal experiments were approved by the Institutional Animal Care and Use

Committee of Shanghai Ninth People's Hospital (No.: SH9H-2026-A1299-1). The CIA mouse model was established as previously described. Bovine type II collagen was first dissolved in 0.05 N acetic acid to a final concentration of 2 mg/mL. This collagen solution was then mixed with complete Freund's adjuvant (CFA) at a 1:1 (v/v) ratio and thoroughly emulsified using a tissue homogenizer to prepare the immunization emulsion. On day 0, 7-week-old DBA/1 mice were anesthetized and received a slow intradermal injection of 100 μL of the emulsion into the tail, approximately 1.5 cm proximal to the tail base. A booster immunization was administered on day 20, consisting of 50 μL of bovine type II collagen emulsified in incomplete Freund's adjuvant (IFA).

In vivo targeting study

CIA mice were randomly divided into three groups: free Por group; CPP group; CPPF group. The mice were injected via the tail vein. In vivo fluorescence imaging was performed at 6, 12, 24, and 48 h post-injection using an IVIS Spectrum imaging system. At 48 h post-injection, the mice were sacrificed, and major organs (heart, liver, spleen, lung, kidney) and hind paws were harvested. Ex vivo fluorescence imaging of the harvested tissues was performed.

In vivo photothermal performance

CIA mice were injected via the tail vein with CPPF NPs. At 24 h post-injection, the inflamed hind paws were irradiated with an 808 nm laser for 5 min. Real-time thermal images were recorded every 1 min using a thermal camera, and the paw temperature was measured.

In vivo therapeutic study

CIA mice were randomly divided into five groups (n = 6 per group): (1) Control (healthy mice without immunization); (2) Saline (CIA mice treated with saline); (3) NPs (CIA mice treated with CPPF NPs only); (4) NPs+660 nm (CIA mice treated with CPPF NPs + 660 nm laser irradiation); (5) NPs+660/808 nm (CIA mice treated with CPPF NPs + sequential 660/808 nm laser irradiation). Treatments were administered

every 3 days for a total of 21 days. For laser irradiation groups, 660 nm-mediated PDT was performed once at 24 h after each injection (i.e., every 3 days) for 3 min to the hind paws, while 808 nm-mediated mild PTT was applied daily for 15 min to the hind paws throughout the entire treatment period. To precisely control the PTT effect and prevent excessive thermal injury, the local temperature of the irradiated paws was continuously monitored in real time using a thermal infrared camera during the entire 808 nm irradiation period, with the temperature strictly controlled below 45 ℃.

Paw thickness was measured using a digital caliper every 3 days. Arthritis score was assessed by two independent observers in a blinded manner according to the following criteria: 0 = no swelling or redness; 1 = slight swelling or redness in one toe; 2 = moderate swelling in multiple toes or paw; 3 = severe swelling of the entire paw; 4 = maximum swelling with joint deformity. Body weight was monitored every 3 days.

At the end of the treatment period, photos and infrared thermal images of the hind paws were taken. The mice were then sacrificed, and the hind paws were harvested for micro-CT scanning and histological analysis. Joint tissue homogenates were prepared, and the concentrations of TNF-α, IL-1β, IL-6, IL-10, and TGF-β were measured by ELISA. Blood samples were collected to perform routine blood tests, and major organs (heart, liver, spleen, lung, kidney) were harvested, fixed in 4% paraformaldehyde, embedded in paraffin, sectioned, and stained with H&E for histological examination.

Statistical analysis

All data were presented as mean ± SD of at least three independent experiments. Statistical analysis was performed using GraphPad Prism 10.1.2 software. Differences between multiple groups were analyzed by one-way ANOVA. Significance levels were set as $*P<0.05$, $**P<0.01$, $***P<0.001$, and $****P<0.0001$.

Results and discussion

Synthesis and characterization of CPPF NPs

The multifunctional CPPF NPs were meticulously engineered through a stepwise

surface engineering and site-specific conjugation strategy (Scheme 1). Initially, the CuTA were synthesized via coordination reaction between Cu^{2+} ions and tannic acid (TA) ligands to serve as the catalytic nanozyme core [37]. Subsequently, a PDA shell was modified onto CuTA surface through the self-polymerization of dopamine hydrochloride, yielding CuTA@PDA (CP) NPs. This PDA layer provided abundant reactive sites (e.g., amino and quinone groups) for further functionalization [38-40]. Specifically, carboxylated porphyrin (Por-COOH) was covalently grafted onto the amino groups of the PDA shell via an EDC/NHS-mediated amide condensation reaction [41], endowing the platform with photodynamic activity. Finally, the targeting ligands (SH-PEG-FA) were integrated onto the PDA surface through a thiol-ene Michael addition reaction. This hierarchical construction culminates in the formation of the final CPPF NPs, a sophisticated nanoplatform tailored for the targeted sequential therapy of RA.

Transmission electron microscopy (TEM) was used to characterize the morphological evolution of the nanoplatform at each synthetic stage. As shown in Figure 1A, the pristine CuTA exhibited a two-dimensional sheet-like morphology. After in situ polymerization of dopamine (Figure 1B), the resulting CP NPs transformed into ellipsoidal-like spherical structures with increased overall size, confirming the formation of PDA layer. The final CPPF NPs (Figure 1C) maintained a core-shell structure, surface became significantly smoother with reduced roughness compared to CP NPs, which is attributed to the modification of the SH-PEG-FA.

Dynamic light scattering (DLS) and zeta potential measurements further corroborated the successful stepwise modification. As shown in Figure 1D, the CuTA NPs exhibited an excessively large hydrodynamic diameter exceeding 1000 nm, despite their small dry-state size observed by TEM. Such poor colloidal stability and aqueous dispersibility would inevitably lead to rapid sedimentation in physiological media and non-specific clearance by the reticuloendothelial system (RES) [42], severely limiting the biological utility of unmodified CuTA. However, PDA coating effectively screened the interparticle hydrogen bonding and electrostatic interactions, drastically reducing the

hydrodynamic diameter to 304.4 nm for CP NPs. Subsequent covalent conjugation of Por-COOH and SH-PEG-FA further decreased the size to 222.1 nm (CPPF NPs). This size reduction was attributed to the dense, hydrated polyethylene glycol (PEG) brush that provides steric stabilization and effectively suppresses nanoparticle agglomeration in complex biological fluids. Consistent with the size variation, zeta potential analysis (Figure 1E) also confirmed the surface modification. CuTA NPs showed a weak negative charge (-8.47 mV), which shifted to -18.3 mV after PDA coating due to negatively charged quinone and hydroxyl groups. Further functionalization yielded CPP (-18.2 mV) and CPPF (-21.9 mV), respectively. This moderate negative surface charge is favorable for in vivo applications, as it effectively minimizes non-specific protein adsorption and prolongs the systemic circulation time of CPPF NPs [43].

Ultraviolet-visible (UV-vis) absorption spectroscopy was performed to verify the successful grafting of photodynamic and targeting moieties. As shown in Figure 1F, CPPF NPs retained all the characteristic absorption peaks of CuTA, PDA and Por (400 nm, and 500–700 nm), and exhibited an additional distinct absorption peak at ~280 nm corresponding to the FA ligand. Based on the characteristic absorption of Por at 575 nm, the entrapment efficiency and drug loading content of Por were quantitatively determined by the standard curve method (Figure S1), which were calculated to be 47.06 ± 4.76% and 4.49 ± 0.43%, respectively. Fourier transform infrared (FTIR) spectroscopy was further used to characterize the chemical structure evolution. As shown in Figure S2, the formation of CuTA coordination complexes was verified by the broadened O-H stretching band and the appearance of a Cu-O stretching peak at ~600 cm^{-1}. The comparison of FTIR spectra between CuTA and the final CPPF NPs (Figure 1G) provided comprehensive evidence for the successful stepwise surface modification. In addition to the retained O-H stretching band (3200–3600 cm^{-1}) and Cu-O stretching peak (~600 cm^{-1}) from the CuTA core, the CPPF spectrum showed several new characteristic peaks: the absorption band at 2800–3000 cm^{-1} was attributed to the C-H stretching vibration of alkyl chains in PDA, Por and PEG; the peaks at 1500–1650 cm^{-1} corresponded to the C=N and C=C stretching vibrations of aromatic rings in

PDA and Por macrocycles; and the multiple peaks in the 1000–1400 cm^{-1} region were assigned to the C-O and C-O-C stretching vibrations from TA, PDA and the ether linkages in PEG. Collectively, these FTIR results confirmed that the CuTA core structure remained intact during the entire surface modification process, and all functional components were covalently integrated into the nanoplatform. X-ray diffraction (XRD) pattern (Figure 1H) further revealed the crystalline phase evolution. The pristine CuTA NPs exhibited distinct diffraction peaks, and after stepwise modification, the characteristic diffraction peaks of CuTA remained at the same 2θ positions, yet showed a significant decrease in intensity. In addition, no new impurity phases or crystalline byproducts were observed.

Raman spectroscopy and X-ray photoelectron spectroscopy (XPS) were used to investigate the interfacial structural evolution. The appearance of the characteristic D and G bands of disordered carbon in the Raman spectrum confirmed the formation of an amorphous PDA layer (Figure 1I) [16]. XPS elemental analysis further corroborated the successful construction of the CPPF (Figure 1J and Figure S3), where the detected N 1s (4.28 at%) and S 2p (2.99 at%) signals were attributed to the nitrogen-containing PDA/Por skeletons and the thiolated PEG-FA ligands, respectively. High-resolution Cu 2p spectra were further scrutinized to elucidate the electronic evolution of the catalytic centers (Figure S3). For CuTA NPs, the Cu 2p3/2 peak was centered at 934.9 eV. Following the interfacial nano-reconstruction driven by PDA and Por, the Cu 2p envelope of CPPF NPs exhibited a significant negative shift of 1.3 eV, with the peak center moving to 933.6 eV. According to the electronic structure modulation principle, this shift indicated a substantial increase in electron density at the copper centers, arising from the strong electron-donating effect of both the phenolic hydroxyl groups of PDA and the newly coordinated nitrogen-containing ligands (pyrrole and amino moieties). Importantly, this structural transformation is not merely a physical mixture of individual functional components but involves the fundamental re-coordination of metal centers, resulting in the formation of CPPF nanozyme.

To further explore the impact of interfacial reconstruction on the porous structure of

CPPF NPs, nitrogen adsorption-desorption isotherms were conducted (Figure 1K). Both samples exhibited typical type IV isotherms with H3-type hysteresis loops in the high relative pressure range. The Brunauer-Emmett-Teller (BET) specific surface area of CuTA was measured at 83.99 $m^2 g^{-1}$. Following the modification, the BET surface area of CPPF decreased by 32.3% to 56.82 $m^2 g^{-1}$.This decline is primarily ascribed to the successful deposition of organic functional layers on the CuTA surface, which preferentially occluded the microporous and small mesoporous channels. Notably, t-plot analysis (Table S1) revealed a negligible internal surface area for both samples, confirming the absence of genuine microporosity. Consequently, the specific surface area originates almost exclusively from the external surface and mesopores. Such a mesopore-dominant configuration is highly conducive to the SOD- and CAT-like catalytic relay, as it ensures the unhindered accessibility of active copper sites to short-lived ROS substrates by eliminating mass transfer resistance, which would otherwise be imposed by microporous constraints.

To evaluate the potential of CPPF NPs as a multifunctional phototherapeutic platform, their ROS generation capability and photothermal effect were systematically investigated under 660 or 808 nm laser irradiation. The PDT effect of CPPF NPs was assessed using 1,3-diphenylisobenzofuran (DPBF) as a sensitive chemical probe. As shown in Figure 1L, upon 660 nm laser irradiation, the characteristic absorbance of DPBF at 410 nm exhibited a rapid, time-dependent decrease over a 5-minute period. This significant quenching indicates the efficient generation of ROS by the Por moieties within the CPPF framework upon light excitation. In contrast, the absorbance of DPBF alone declined slightly under the same conditions (Figure S4). Notably, DPBF depletion became negligible after 3 min of irradiation, suggesting that ROS generation had reached a plateau. To avoid over-irradiation and potential light-induced side effects, we set the laser exposure time to 3 min in all subsequent PDT studies. Next, the PTT performance and PTT stability of CPPF NPs were investigated using a precision thermometer and infrared thermal imaging camera. Under 808 nm laser irradiation, the CPPF aqueous solutions exhibited a distinct concentration-dependent temperature rise

(Figure 1M), the temperature of the 400 μg/mL group increased by 27.1 ℃ within 600 s. The result in Figure S5A revealed that CPPF NPs possessed a significantly higher heating rate and steady-state temperature compared to PBS group, and thermal imaging (Figure 1N) visually corroborated these results. High photostability ensures consistent performance during repeated treatments, and the robustness of CPPF NPs was validated through heating-cooling cycles. Results showed that the PTT performance of CPPF decreased by only approximately 7% after four consecutive heating–cooling cycles (Figure 1O), and declined by about 30% after four cycles with 1-day intervals (Figure S5B), confirming the favorable PTT stability of CPPF.

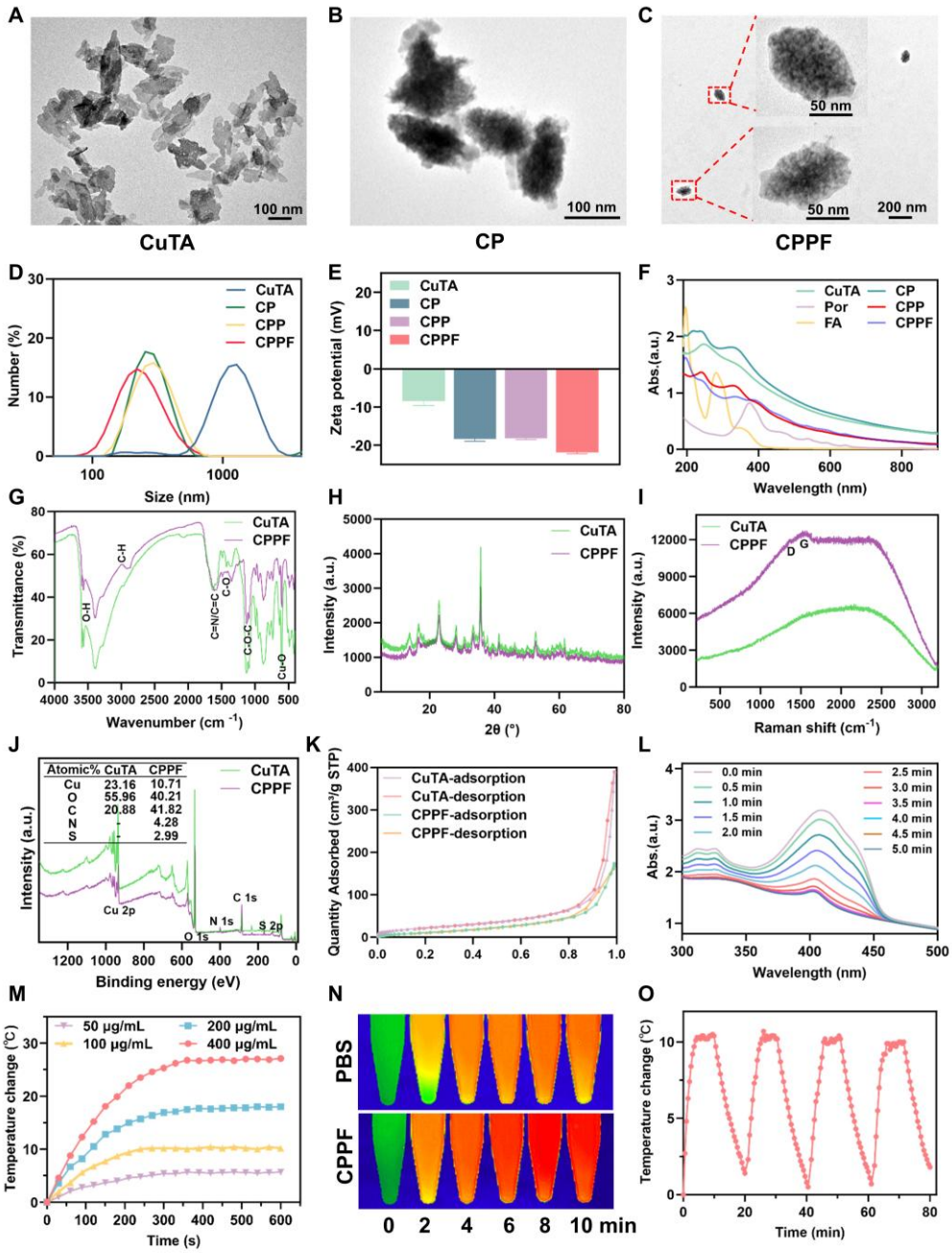


Figure 1. Physicochemical, PDT, and PTT characterization of the CPPF. (A) TEM image of CuTA, (B) CP, and (C) CPPF NPs. (D) Hydrodynamic size distributions of CuTA, CP, CPP, and CPPF measured by DLS. (E) Zeta potentials of CuTA, CP, CPP, and CPPF. (F) UV-vis absorption spectra of CuTA, Por, FA, CP, CPP and CPPF. (G) FTIR spectra, (H) XRD patterns, (I) Raman spectra, (J) XPS survey spectra, and (K) Nitrogen adsorption-desorption isotherms of CuTA and CPPF. (L) The absorption spectra of DPBF in CPPF solution under 660 nm laser irradiation. (M) Photothermal

heating curves of CPPF NPs at different concentrations under 808 nm laser irradiation. (N) Infrared thermal images of PBS and CPPF NP solutions under 808 nm laser irradiation. (O) Photothermal stability of CPPF NPs over four consecutive heating-cooling cycles under 808 nm laser irradiation.

Antioxidant and enzymatic activity characterization of CPPF NPs

To counteract the chronic oxidative stress characteristic of the inflammatory microenvironment, the multi-enzyme mimetic activities of the CPPF NPs were evaluated. As shown in Figures 2A and 2B, CPPF NPs exhibited significant total antioxidant capacity, demonstrating a potent, concentration-dependent free radical scavenging effect. The SOD-like activity of CPPF NPs was assessed using the WST-8 assay. Consistent with the ABTS results, the absorption peak of the WST-8 formazan product at 450 nm decreased gradually with increasing CPPF concentration (Figure 2C), and the quantitative data revealed a concentration-dependent enhancement of $^{\bullet}O^{2-}$ inhibition rate (Figure 2D). Subsequently, the CAT-like activity of CPPF NPs was determined using a catalase assay kit. Similarly, the the characteristic absorption peak at 520 nm gradually decreased with increasing CPPF concentration, verifying the H_2O_2 elimination capacity (Figure 2E, 2F). To further elucidate the underlying mechanism of the enzyme-mimicking activity of CPPF NPs, cyclic voltammetry (CV) measurement was performed. As shown in Figure S6, the CV curve of CPPF NPs displayed distinct redox peaks within the potential range of 0–2.2 V (vs. SHE), which corresponded to the reversible valence transition between Cu^{+} and Cu^{2+} [44]. This reversible redox cycle is the intrinsic basis for the SOD-like and CAT-like activities of CPPF NPs, which mediates the cascade scavenging of ROS through electron transfer processes.

As a sophisticated nano-regulator designed for spatiotemporal ROS modulation, integrating light-triggered ROS generation with subsequent enzymatic elimination, the preservation of catalytic integrity following PDT is of paramount importance. The analysis of CuTA, CPPF, and laser-pretreated CPPF (CPPF+L, 660 nm for 3 min) revealed that the surface engineering process led to an enhancement in SOD-like activity for CPPF compared to CuTA, while the CAT-mimetic performance remained

consistent (Figures 2G-I). This suggests that modification optimizes the electronic environment of the copper active sites for superoxide disproportionation. Most importantly, while the CPPF+L group exhibited a slight decline in enzymatic activity due to the initial photodynamic consumption of active sites, it successfully retained the vast majority of its antioxidant capacity (Figures 2G-I). This function serves as the essential foundation for the sequential ROS regulation, ensuring it can execute targeted PDT while concurrently providing long-term protection against inflammatory oxidative stress. The ROS modulation of the CPPF NPs were further validated at the cellular level using lipopolysaccharide (LPS)-induced inflammation model monitored by the DCFH-DA fluorescence probe. As depicted in Figure 2J, LPS triggered intense green fluorescence within the RAW 264.7 cells, signifying a sharp elevation in endogenous ROS levels. Subsequent treatment with CPPF NPs resulted in a marked, dose-dependent attenuation of the fluorescence signal, confirming the NPs' high efficiency in clearing intracellular oxidative species. Most importantly, the experimental group treated with laser-preirradiated CPPF NPs (CPPF+L) still exhibited intracellular ROS scavenging capabilities. This finding demonstrates that after undergoing 660 nm laser irradiation for 3 min, the CPPF NPs maintain their antioxidant performance. Such functional persistence ensures that the nanoplatform can serve as a reliable, spatiotemporal regulator capable of executing PDT and restoring the redox balance within inflamed cellular compartments.

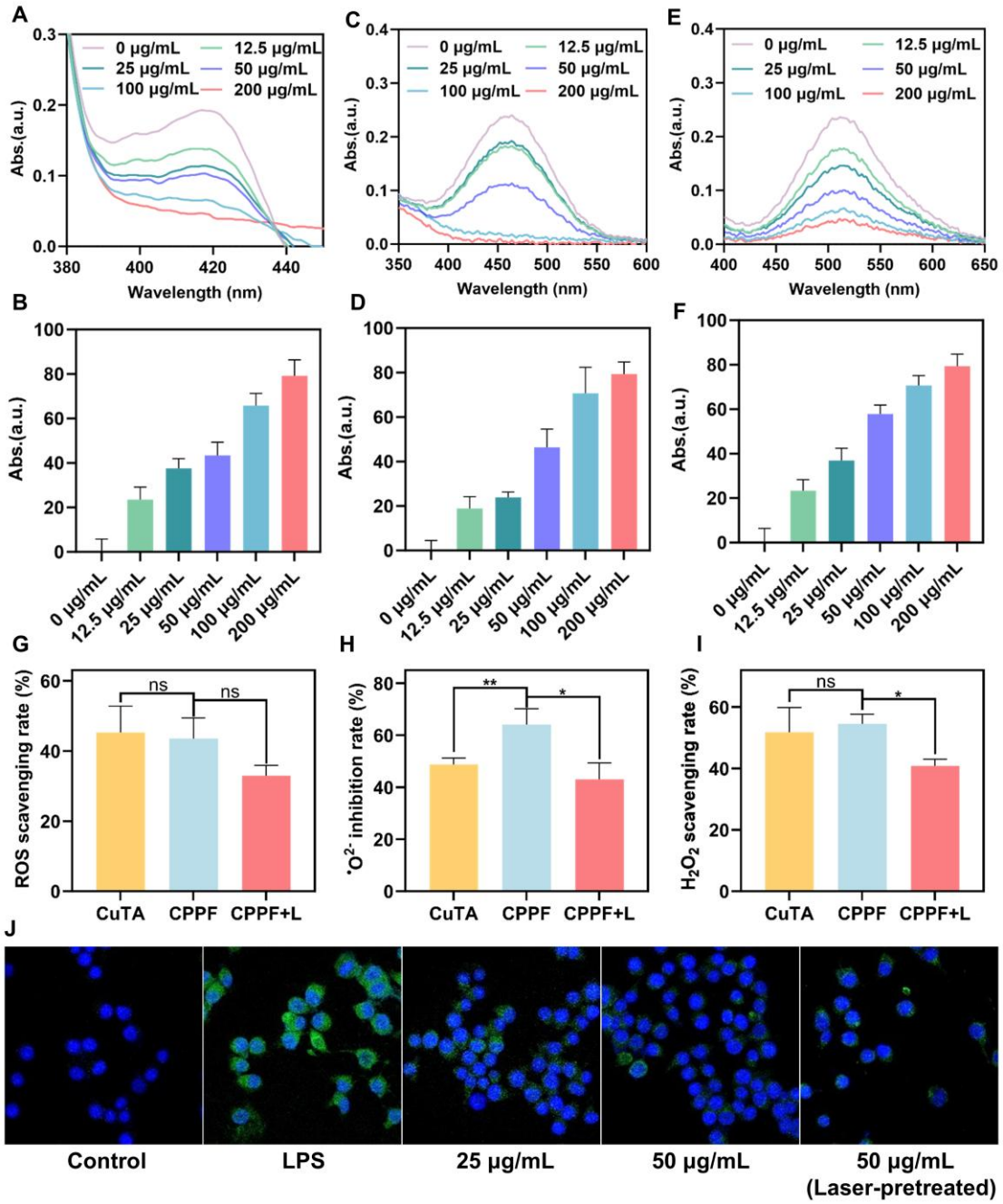


Figure 2. Antioxidant and SOD/CAT activities of the CPPF. (A) UV-vis absorption spectra and (B) quantitative analysis of ABTS radical solutions treated with different concentrations of CPPF. (C) UV-vis absorption spectra and (D) quantitative analysis of WST-8-based SOD-like activity assay, showing formazan product absorbance at 450 nm for different CPPF concentrations. (E) UV-vis absorption spectra and (F) quantitative analysis of CAT-like activity assay, showing residual H_2O_2-derived chromogenic product absorbance at 520 nm for different CPPF concentrations. (G)

Comparison of total ROS scavenging rates, (H) superoxide anion inhibition rates and (I) hydrogen peroxide scavenging rates of CuTA, CPPF, and laser-pretreated CPPF (CPPF+L). (J) CLSM images of intracellular ROS levels in RAW 264.7 macrophages (green: DCFH-DA; blue: Hoechst 33342). Statistical significance between groups was determined using one-way ANOVA, where * $p < 0.05$.

Biocompatibility, cellular uptake, and intracellular PTT/PDT performance of CPPF NPs

Having established the physicochemical properties, dual enzyme-mimetic activities, and in vitro PDT/PTT capabilities of CPPF NPs, we next evaluated their biocompatibility, targeting specificity, and intracellular therapeutic efficacy in M1-polarized macrophages, which are the key effector cells in RA pathogenesis.

The biosafety profile of CPPF NPs was first assessed via CCK-8 assay and hemolysis test. As shown in Figure 3A, CPPF NPs exhibited negligible cytotoxicity against both RAW 264.7 macrophages and ATDC5 chondrocytes at concentrations up to 100 μg/mL after 24 h incubation. The hemocompatibility evaluation further confirmed the safety of CPPF NPs, no significant hemolysis was observed across tested concentrations from 25 to 150 μg/mL (Figure 3B), which meets the standard for intravenous injection.

Subsequently, the cellular uptake behavior of CPPF NPs by M1-polarized macrophages was investigated using confocal laser scanning microscopy (CLSM) and flow cytometry. CLSM images revealed that the red fluorescence of CPPF gradually increased in the cytoplasm of M1 macrophages with prolonged incubation time (Figure 3D). Flow cytometry analysis also demonstrated this time-dependent increase (Figure 3C), confirming efficient internalization of CPPF NPs by M1 macrophages. To verify the FA-mediated targeting effect, we compared the cellular uptake of CPPF NPs with CPP NPs (without FA modification) and the free FA-preblocked group. As shown in Figure 3F, after incubation, the MFI of the CPPF group was significantly higher than that of the CPP group, while pre-incubation with free FA inhibited the cellular uptake of CPPF NPs, demonstrating that the internalization was mediated by folate receptor-

mediated endocytosis. Notably, flow cytometry analysis further revealed that CPPF NPs exhibited preferential uptake by M1-polarized macrophages compared to M0 and M2 phenotypes (Figure S7), which is desirable for targeted therapy of RA, as M1 macrophages are the major pro-inflammatory cells infiltrating the inflamed joints.

The intracellular mild photothermal effect of CPPF NPs was subsequently investigated under 808 nm laser irradiation. Thermal imaging demonstrated that CPPF NPs exhibited a cell phenotype-dependent mild photothermal effect in different cell populations (Figure 3G). Specifically, after 5 min of laser irradiation, the PBS control group showed insignificant temperature fluctuation, while M0 macrophages incubated with CPPF NPs exhibited a moderate temperature increase. However, M1-polarized macrophages that preferentially take up CPPF NPs reached a peak temperature of 45.3 ℃. This temperature elevation falls within the range of mild hyperthermia (42–46 ℃), which avoids non-specific thermal damage to cells but can effectively modulate cellular biological functions [45, 46]. This differential temperature elevation between M0 and M1 macrophages was consistent with our cellular uptake results, confirming that the targeted accumulation of CPPF NPs in pro-inflammatory M1 macrophages enables selective mild photothermal modulation of pathological cells while minimizing off-target effects on normal cells. To corroborate the induction of intracellular mild PTT at the molecular level, we examined the expression of HSP70, a well-established and sensitive biomarker of cellular thermal response. Notably, HSP70 not only functions as a molecular chaperone to protect cells from irreversible protein denaturation under thermal stress but also exerts intrinsic anti-inflammatory effects by negatively regulating the NF-κB signaling pathway and downregulating the production of pro-inflammatory cytokines. Western blot analysis revealed that the combination of CPPF NPs and 808 nm laser irradiation resulted in HSP70 upregulation (Figure 3H). These findings collectively provide direct molecular evidence for intracellular mild PTT of CPPF NPs. This mild PTT effect can synergize with the intrinsic antioxidant and dual enzyme-mimicking activities of CPPF NPs: mild hyperthermia can enhance the catalytic activity of nanozymes, while the upregulated HSP70 can further augment the

anti-inflammatory and antioxidant effects, forming a synergistic therapeutic network to alleviate oxidative stress and inflammation in RA microenvironment.

The cytotoxicity of CPPF NPs-mediated PDT to M1-type RAW 264.7 macrophages was first evaluated using the CCK-8 assay (Figure 3I). After 3 min of 660 nm laser irradiation, CPPF NPs exhibited a dose-dependent cytotoxic effect on M1 macrophages. As the concentration increased to 50 μg/mL and 100 μg/mL, cell viabilities decreased to 28.42% and 11.49%, respectively. These results demonstrated that CPPF NPs can effectively kill pro-inflammatory M1 macrophages in a concentration-dependent manner under 660 laser irradiation. To further verify that the reduced cell viability was attributed to apoptosis, we performed Annexin V-FITC/PI staining flow cytometry analysis (Figure 3J). Quantitative analysis of apoptotic cell populations (Figure S8) revealed that the control, laser irradiation, and NPs alone groups exhibited negligible levels of apoptosis, with total apoptotic rates of only 0.62%, 1.20%, and 2.93%, respectively (Figure 3K). In contrast, the NPs + 660 nm PDT group showed a dramatic increase in apoptotic cell percentage, reaching 64.90% after treatment. This apoptotic effect is attributed to the intracellular generation of cytotoxic ROS by CPPF NPs upon 660 nm laser excitation. The NPs + 660/808 nm combined treatment group exhibited a comparable apoptotic rate of 65.39%, further confirming that the 808 nm mild PTT effect does not enhance the apoptotic effect of PDT.

From the perspective of RA therapeutic strategy, selective elimination of hyperactivated M1 macrophages represents a cornerstone for alleviating joint inflammation and preventing tissue destruction. Compared with conventional systemic chemotherapy, PDT offers advantages of spatiotemporal controllability and targeted cytotoxicity. It specifically induces apoptosis in M1 macrophages that have preferentially taken up CPPF NPs, while minimizing off-target damage to normal cells and tissues. In our study, the efficient M1 macrophage apoptosis induced by CPPF NPs-mediated PDT effectively eliminates the primary source of pro-inflammatory cytokines in the RA microenvironment. Meanwhile, the 808 nm mild PTT further upregulates the expression of anti-inflammatory HSP70, forming a complementary therapeutic network

of “PDT-mediated pathological cell clearance + mild PTT-assisted anti-inflammatory modulation”.

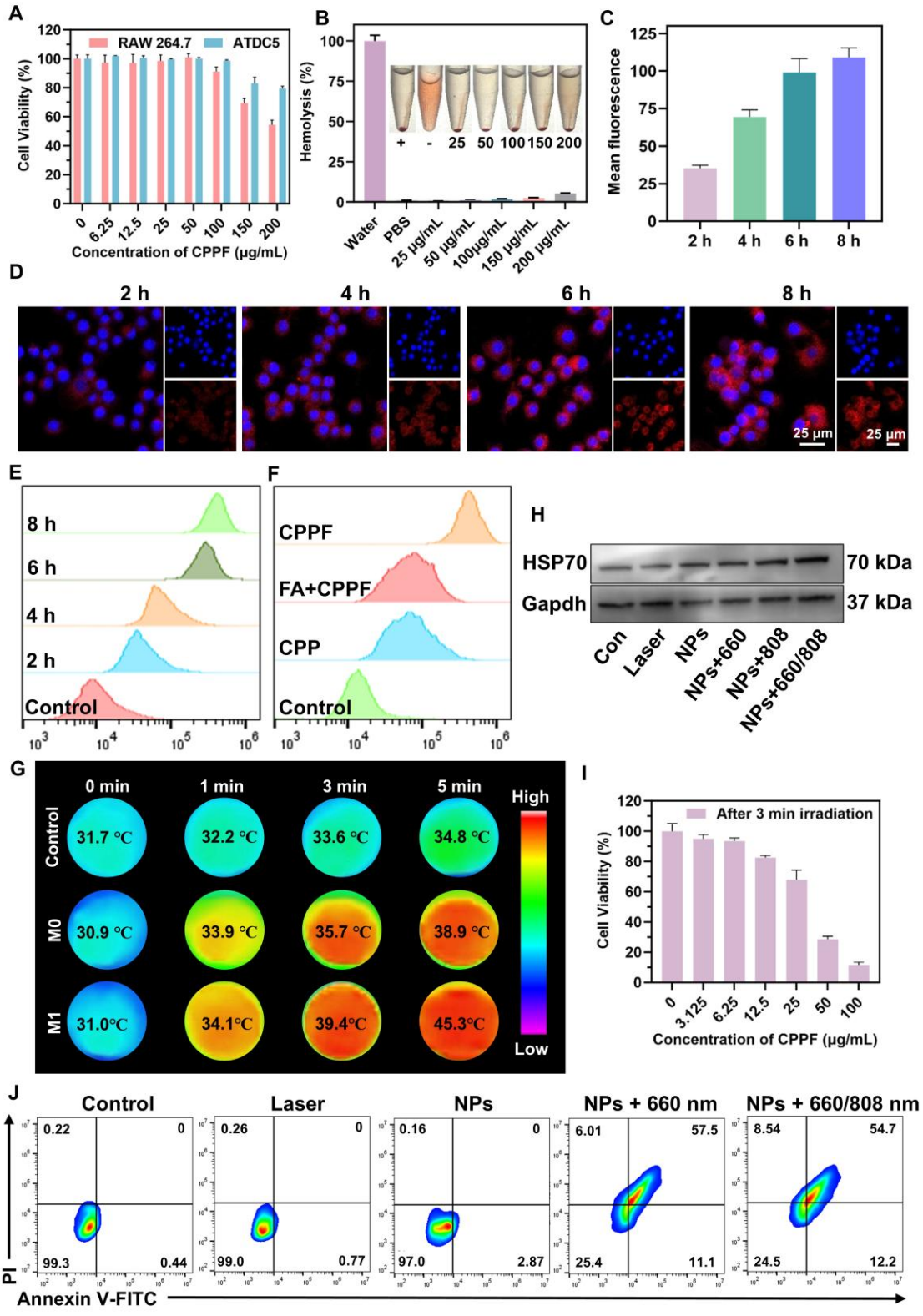


Figure 3. (A) Cell viabilities of RAW 264.7 macrophages and ATDC5 chondrocytes

after 24 h incubation with different concentrations of CPPF. (B) Hemolysis rates of mouse RBCs treated with different concentrations of CPPF and corresponding digital photographs. (C) Quantitative analysis and (D) CLSM images of time-dependent cellular uptake of CPPF NPs by M1-polarized macrophages (red: Por; blue: DAPI). (E) Flow cytometry histograms of time-dependent CPPF uptake by M1 macrophages, and (F) FA-mediated targeting verified by free FA competition assay. (G) Infrared thermal images of control, M0, and M1-polarized macrophages under 808 nm laser irradiation for 5 min. (H) Western blot of HSP70 protein expression in M1-polarized macrophages after different treatments. (I) Cytotoxicity of CPPF NPs against M1-polarized macrophages under 660 nm laser irradiation for 3 min. (J) Flow cytometry analysis of M1-polarized macrophage apoptosis detected by Annexin V-FITC/PI staining after different treatments.

Sequential phototherapy-enzymatic therapy mediated by CPPF NPs modulates macrophage polarization and inflammatory responses

While monotherapies including PDT and PTT have demonstrated efficacy in eliminating inflammatory cells, they often fail to simultaneously remodel the immunosuppressive microenvironment, leading to persistent inflammation and disease recurrence. In this section, we evaluated the effect of sequential phototherapy-enzymatic therapy mediated by CPPF NPs.

To validate the reliability of the macrophage polarization model, RAW 264.7 cells were polarized to the M1 phenotype using LPS and to the M2 phenotype using IL-4. Immunofluorescence staining revealed that LPS stimulation significantly enhanced the fluorescence intensity of the M1 marker iNOS, while IL-4 treatment markedly upregulated the expression of the M2 marker CD206, confirming the successful construction of the polarization model (Figure S9). The regulatory effects of different treatment modalities on macrophage polarization were first evaluated by CLSM. As shown in Figures 4A and 4B, LPS stimulation resulted in a substantial increase in iNOS fluorescence intensity, which gradually decreased in NPs, NPs + 660 nm, and NPs + 660/808 nm groups. Conversely, CD206 fluorescence intensity was significantly

enhanced in the NPs + 660/808 nm group compared with other treatment groups. Quantitative analysis also confirmed these observations (Figure S10). Western blot of iNOS protein expression (Figure S11) provided additional evidence for the polarization regulatory effect, showing that sequential therapy led to a significant inhibition of M1 polarization.

Flow cytometry was subsequently performed to verify the polarization regulatory effect. As shown in Figures 4C and 4D, untreated M0 macrophages exhibited low expression levels of both the M1 surface marker CD86 (3.13%) and the M2 surface marker CD206 (2.81%). Following LPS stimulation, the proportion of $CD86^+$ cells sharply increased to 40.81%, while CD206 expression remained at basal levels (2.61%), confirming successful M1 polarization. Quantitative analysis (Figure 4E) demonstrated that treatment with CPPF NPs alone (NPs group) partially reversed this phenotype, reducing the proportion of $CD86^+$ cells to 25.96% and increasing the proportion of $CD206^+$ cells to 17.94%, indicating that CPPF nanozymes possess intrinsic immunomodulatory activity. Monotherapy with PDT (NPs + 660 nm group) further enhanced this effect, with the proportion of $CD86^+$ cells decreasing to 14.42% and $CD206^+$ cells increasing to 23.69%. This observation can be attributed to the selective elimination of M1 macrophages by ROS generated during PDT. Notably, sequential therapy (NPs + 660/808 nm group) achieved the most significant polarization regulatory effect: the proportion of $CD86^+$ cells decreased to 12.22%, while the proportion of $CD206^+$ cells increased to 30.63%, demonstrating the superior advantage of the cascade therapeutic strategy in promoting M1-to-M2 phenotypic transition.

To assess the functional consequences of macrophage polarization reprogramming, the secretion levels of key inflammatory cytokines were measured by ELISA. As shown in Figures 4F–4J, LPS stimulation led to a dramatic increase in the secretion of pro-inflammatory cytokines TNF-α, IL-6, and IL-1β. Treatment with CPPF alone or monotherapy with PDT partially reversed this cytokine profile, while sequential therapy exhibited the most potent anti-inflammatory effect: the levels of IL-6, IL-1β, and TNF-α decreased to 11.67 pg/mL, 3.47 pg/mL, and 3.41 pg/mL, respectively, while the levels

of IL-10 and TGF-β increased to 29.10 pg/mL and 44.19 pg/mL, respectively.

The superior therapeutic efficacy of the sequential cascade strategy can be attributed to the synergistic action of three interrelated mechanisms: PDT triggered by 660 nm laser irradiation generates ROS, selectively inducing apoptosis of overactivated M1 macrophages and rapidly reducing the source of pro-inflammatory mediators; the intrinsic SOD/CAT cascade antioxidant activity of CPPF scavenges residual intracellular ROS; mild PTT activated by 808 nm laser irradiation upregulates the expression of HSP70, which further promotes macrophage differentiation toward the M2 phenotype. This “elimination followed by remodeling” approach effectively breaks the vicious cycle of inflammation and oxidative stress, achieving comprehensive immunomodulation.

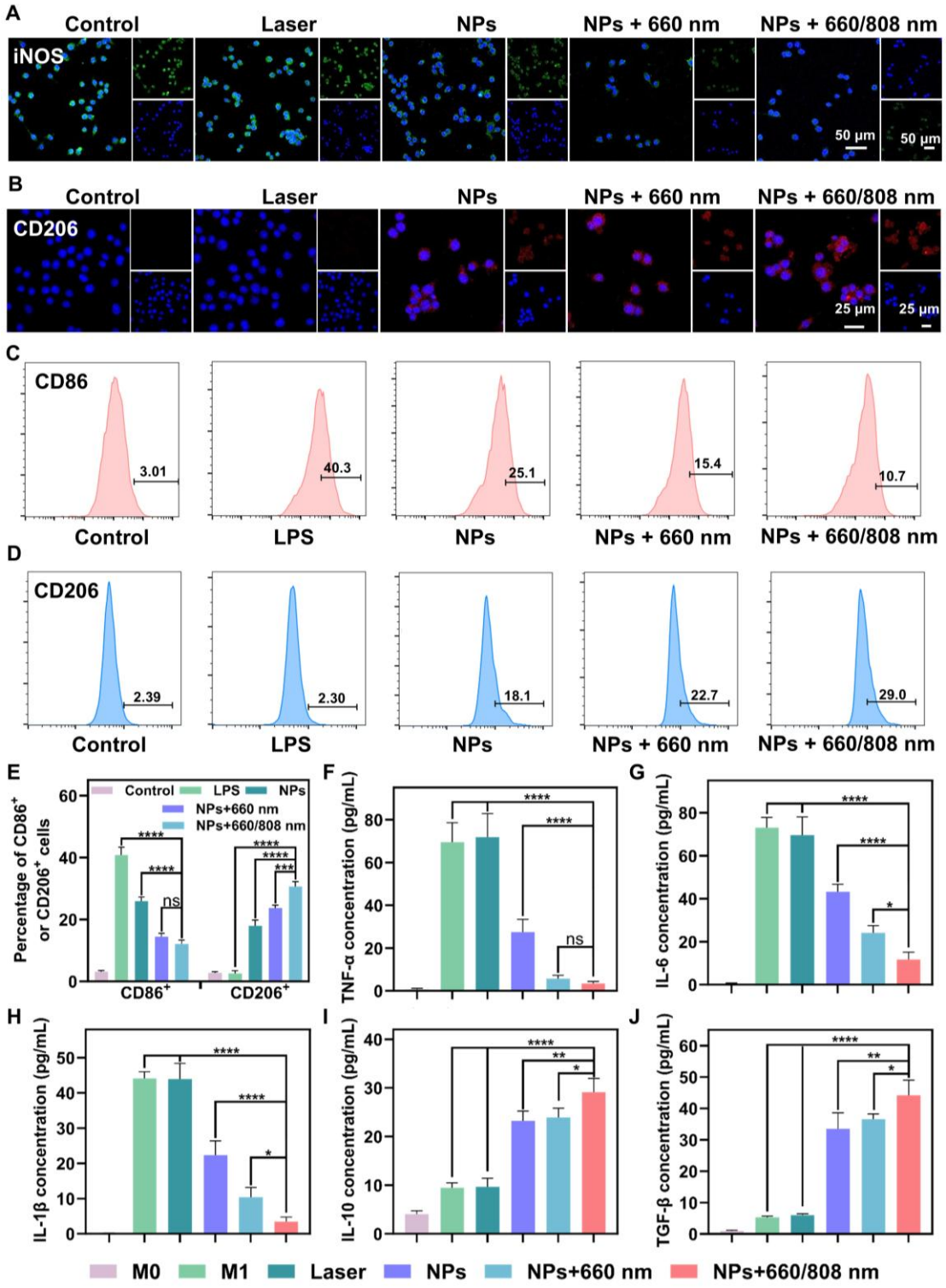


Figure 4. Macrophage polarization regulation and anti-inflammatory effects of CPPF NPs in vitro. (A) CLSM images of iNOS (green) and (B) CD206 (red) expression in RAW 264.7 macrophages after different treatments (blue: DAPI). (C) Flow cytometry histograms of CD86 and (D) CD206 (M2) expression, and quantitative analysis in RAW 264.7 macrophages after different treatments. (F) ELISA analysis of pro-inflammatory

cytokine IL-6, (G) IL-1β, (H) TNF-α and anti-inflammatory cytokines (I) IL-10, (J) TGF-β secretion levels in cell supernatants after different treatments. Statistical significance between groups was determined using one-way ANOVA, where * $p < 0.05$, ** $p < 0.01$, *** $p < 0.001$, and **** $p < 0.0001$.

Transcriptomic analysis of CPPF-mediated immunomodulation and PDT effects

Building upon the in vitro functional evidence of macrophage polarization reprogramming, we performed RNA-sequencing (RNA-seq) to dissect the underlying molecular mechanisms of CPPF-mediated immunomodulation and PDT. LPS-induced RAW 264.7 macrophages were divided into three groups: Control (LPS only), NPs (LPS + CPPF), and NPs+L (LPS + CPPF + 660 nm laser irradiation). Principal component analysis (PCA) revealed clear transcriptomic separation among the three groups, with the NPs+L group exhibiting the most distinct profile (Figure 5A). Volcano plot analysis further quantified differentially expressed genes (DEGs): compared with the Control group, both NPs group and NPs+L group showed significantly transcriptomic changes (Figures 5B, 5C). Consistent with the macrophage polarization results in Section 2.4, Gene Ontology (GO) enrichment analysis of the NPs vs. Control comparison revealed significant downregulation of immune-related biological processes, including regulation of immune system process, cytokine production, and leukocyte activation (Figure 5D). Kyoto Encyclopedia of Genes and Genomes (KEGG) pathway analysis further confirmed the suppression of pro-inflammatory signaling cascades, such as the TNF signaling pathway, NF-κB signaling pathway, and the rheumatoid arthritis pathway (Figure 5E). These findings provided molecular-level validation of the functional observations, where CPPF treatment alone reduced pro-inflammatory cytokine secretion and skewed macrophages toward an anti-inflammatory phenotype.

To further verify the regulatory effects on macrophage polarization and redox homeostasis, we performed heatmap analysis of key gene sets (Figure 5F). Consistent with flow cytometry and immunofluorescence data, M1 macrophage markers (*Il6*, *Il1b*, *Cd86*) were downregulated in the NPs group, while M2 markers (*Il10*, *Arg1*, *Mrc1*)

were upregulated. Concurrently, genes encoding components of the TNF/NF-κB signaling axis were suppressed, and antioxidant response genes (*Hmox1*, *Nqo1*, *Gclm,* and *Gsta2*) were upregulated. This transcriptional signature aligns perfectly with the intrinsic SOD/CAT cascade antioxidant activity of CPPF nanozymes, which scavenge intracellular ROS and thereby inhibit ROS-mediated NF-κB activation.

Supplementary heatmap analysis of matrix degradation-related genes (Figure S12) further revealed that key extracellular matrix (ECM) degrading enzymes, including Mmp3, Mmp9, Mmp12, and Mmp13, were significantly downregulated after CPPF treatment. Concomitantly, genes encoding collagens (*Col14a1*, *Col15a1*) and integrins (*Itga4*, *Itgb4*) involved in ECM remodeling were also modulated. This transcriptional reprogramming indicates that CPPF nanozymes not only regulate macrophage polarization but also directly suppress the matrix-degrading capacity of M1 macrophages, laying a molecular foundation for the subsequent chondroprotective effects. Consistently, heatmap analysis of oxidative stress-related genes provided comprehensive transcriptomic validation of the antioxidant activity of CPPF nanozymes (Figure S13). *Nrf2* downstream antioxidant and phase II detoxification enzymes, including *Hmox1*, *Nqo1*, *Gsta2*, *Gsta3*, *Gstm1*, *Gstp2*, and *Gclm*, were significantly upregulated in the NPs group. These findings confirm that CPPF nanozymes effectively alleviate intracellular oxidative stress in activated macrophages by activating the Nrf2-mediated antioxidant defense system [47].

To elucidate the molecular mechanisms underlying PDT-induced selective apoptosis of hyperactivated M1 macrophages, we performed transcriptomic analysis of the NPs+L vs. Control comparison. GO enrichment analysis of DEGs revealed significant enrichment in fundamental biological processes essential for apoptosis execution, including cellular process, metabolic process, cellular metabolic process, and biosynthetic process (Figure S14). This transcriptional variation reflects the robust cellular stress response triggered by PDT-generated ROS, which drives the activation of multiple apoptotic signaling cascades. Consistently, KEGG pathway analysis identified the core signaling networks mediating this process, with the chemical

carcinogenesis-reactive oxygen species pathway being significantly enriched, confirming that intracellular ROS accumulation is the important event of PDT-induced cell death. Heatmap analysis of apoptosis-related gene sets provided a view of the apoptotic transcriptional program (Figure S15). In contrast to the Control group, the NPs+L group displayed a multi-faceted pro-apoptotic transcriptional signature. Specifically, key anti-apoptotic genes of the inhibitor of apoptosis protein (IAP) family—including *Birc2*, *Birc6*, and *Xiap*—were significantly downregulated, relieving the intrinsic brake on apoptosis execution. Concurrently, genes driving the mitochondrial/intrinsic apoptosis pathway (*Gadd45b*, *Gadd45g*, *Dedd2*, *Dapk2*) and the JNK-mediated stress signaling cascade (*Mapk10*, *Fos*, *Jun*) were markedly upregulated, forming a synergistic pro-apoptotic signaling axis. Notably, genes associated with the extrinsic death receptor pathway showed no induction, indicating that NPs+L-induced apoptosis is independent of extrinsic signaling. These transcriptomic data demonstrate that PDT triggers apoptosis in hyperactivated M1 macrophages through ROS-initiated activation of the intrinsic mitochondrial apoptosis pathway, amplified by JNK stress signaling and derepressed by suppression of IAP family anti-apoptotic genes. This multi-pronged, intrinsic apoptosis mechanism ensures efficient and selective elimination of pro-inflammatory M1 macrophages, underpinning the therapeutic efficacy of our sequential “apoptosis induction-immunomodulation” strategy.

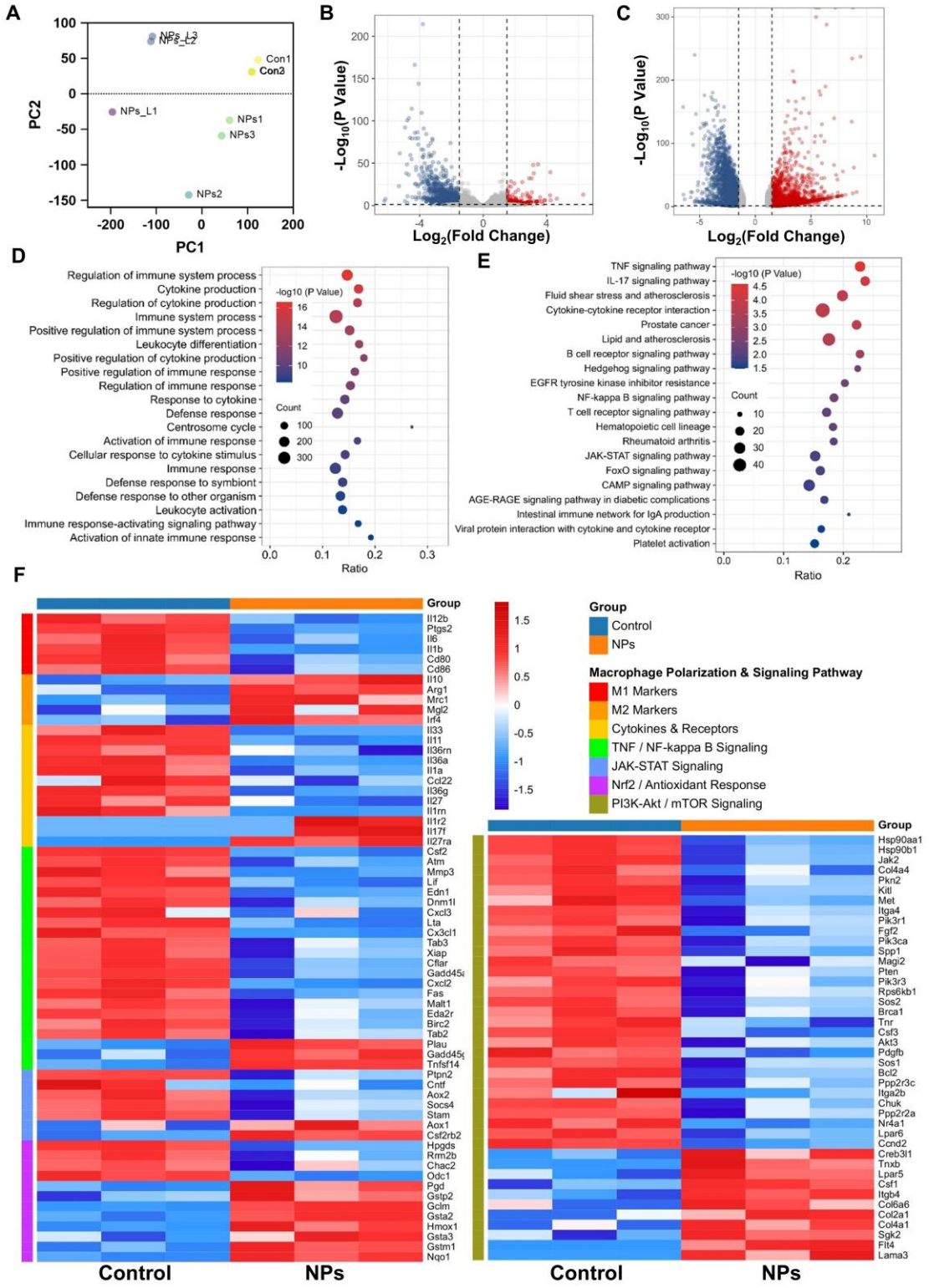


Figure 5. (A) PCA of transcriptomic profiles. (B) Volcano plots of DEGs in NPs vs Control and (C) NPs+L vs Control groups. (D) GO enrichment and (E) KEGG pathway enrichment of NPs vs Control groups. (F) Heatmaps of key genes involved in macrophage polarization and related signaling pathways in control vs NPs groups.

Macrophage reprogramming by CPPF NPs mediates chondroprotection via paracrine cytokine regulation

Building upon the evidence that CPPF-mediated sequential therapy reshapes macrophage phenotype and function, we established a transwell co-culture system to investigate the indirect chondroprotective effects of reprogrammed macrophages, mimicking the paracrine interactions in RA microenvironment (Figure 6A). In this model, RAW 264.7 macrophages were first polarized to M1 phenotype and treated with different regimens, then co-cultured with chondrogenic cells in the lower compartment, allowing free diffusion of soluble cytokines and mediators without direct cell-cell contact [48].

We first evaluated the viability of ATDC5 chondrocytes and bone marrow mesenchymal stem cells (BMSCs) after co-culture with differentially treated macrophages (Figures 6B and 6C). Compared to co-culturing with M0 macrophages, untreated M1 macrophages resulted in a significant decrease in cell viability in both cell types, while CPPF treatment alone, CPPF+PDT, and sequential therapy gradually alleviated M1-induced cell damage, with the sequential therapy group exhibiting the most potent protective effect and restoring cell viability to near-normal levels.

To further investigate the effects of CPPF-reprogrammed macrophages on chondrocyte anabolic and catabolic metabolism, we performed Western blot analysis of three core cartilage homeostasis markers in ATDC5 cells (Figures 6D, 6E). MMP13 is the primary matrix metalloproteinase responsible for the degradation of type II collagen, the major structural component of articular cartilage, and its overexpression is a hallmark of pathological cartilage destruction. In contrast, Col2a1 encodes type II collagen, the defining extracellular matrix protein of hyaline cartilage, and Sox9 is the master transcription factor that regulates chondrocyte differentiation and directly drives Col2a1 expression, both serving as gold standard markers of chondrocyte anabolic activity. Consistent with the pro-catabolic state induced by inflammatory macrophages, co-culture with untreated M1 macrophages dramatically upregulated MMP13 expression and concomitantly downregulated both Sox9 and Col2a1 in ATDC5 cells,

indicating an imbalance between cartilage matrix degradation and synthesis. Treatment with CPPF partially reversed this metabolic dysregulation, while sequential therapy exhibited the most potent corrective effect: MMP13 expression was significantly suppressed, Sox9 and Col2a1 levels were substantially restored.

This restoration of cartilage metabolic homeostasis was mediated by the reshaped inflammatory microenvironment resulting from macrophage reprogramming. To confirm this paracrine mechanism, we measured the concentrations of key inflammatory cytokines in the co-culture supernatant (Figure 6F). Co-culture with untreated M1 macrophages led to massive secretion of pro-inflammatory cytokines TNF-α and IL-1β, which are known to directly induce chondrocyte apoptosis and upregulate matrix-degrading enzymes [49, 50]. In contrast, the sequential therapy group showing the most significant reduction in TNF-α and IL-1β levels. Concomitantly, the level of the key anti-inflammatory cytokine IL-10 was markedly increased in the sequential therapy group.

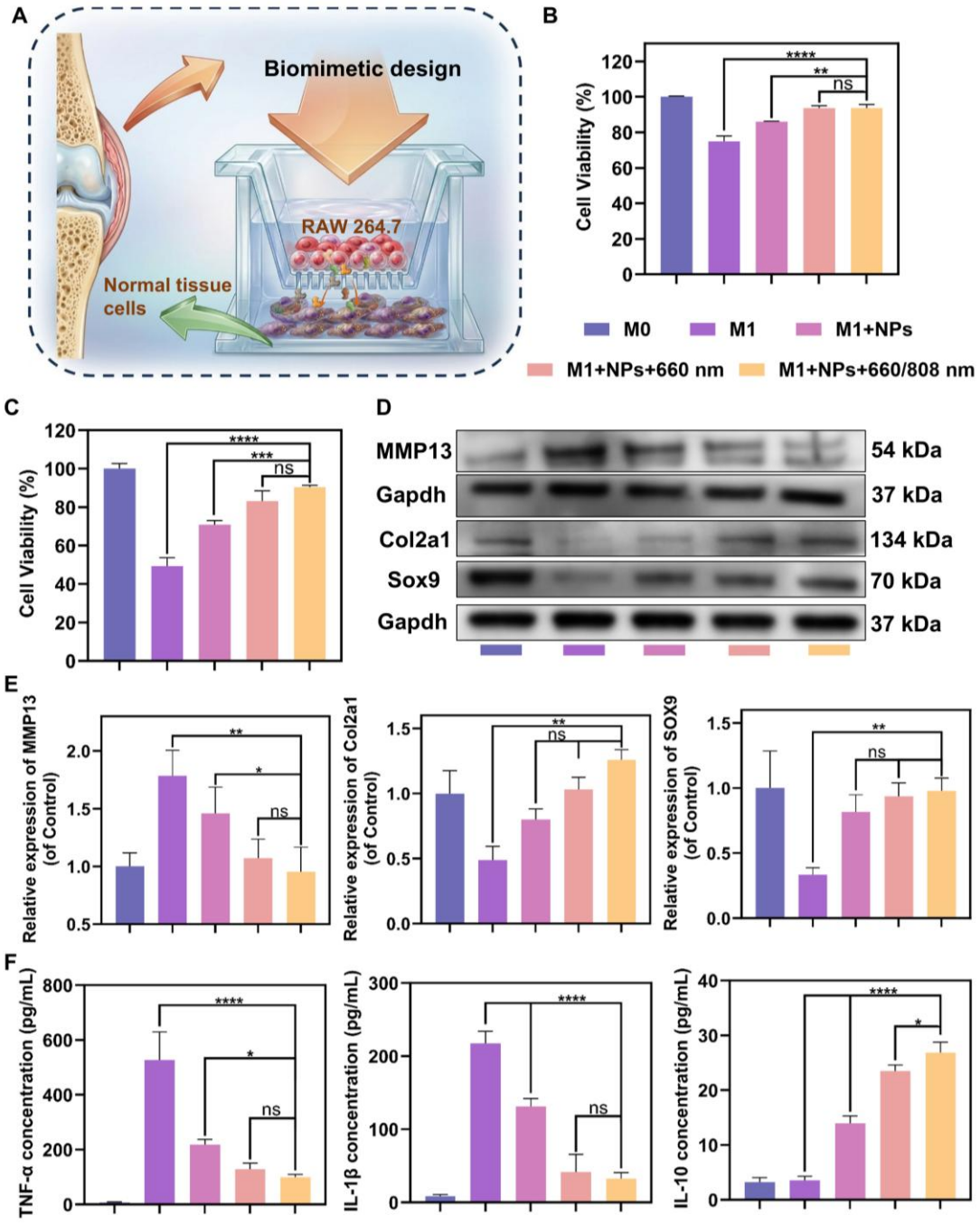


Figure 6. Chondrocyte protective effects of CPPF NPs in a biomimetic co-culture system. (A) Schematic illustration of the biomimetic co-culture system mimicking the RA joint microenvironment. (B) Cell viabilities of ATDC5 chondrocytes and (C) BMSCs co-cultured with differently treated M1-polarized macrophages. (D) Western blot and (E) quantitative analysis of MMP13, Col2a1, and Sox9 protein expression in ATDC5 chondrocytes. (F) ELISA analysis of TNF-α, IL-1β, and IL-10 concentrations in the co-culture supernatants. Statistical significance between groups was determined

using one-way ANOVA, where * $p < 0.05$, ** $p < 0.01$, *** $p < 0.001$, and **** $p < 0.0001$.

In vivo therapeutic efficacy of CPPF-mediated sequential phototherapy-enzymatic therapy in CIA Mice

Building upon in vitro immunomodulatory and chondroprotective effects of CPPF-mediated sequential therapy, we next established a collagen-induced arthritis (CIA) mouse model to systematically evaluate the in vivo targeting capability, photothermal performance, therapeutic efficacy, and biosafety of CPPF NPs [51, 52].

Sufficient and sustained accumulation at arthritic lesions is a cornerstone for achieving therapeutic benefits with nanomedicine in RA. To investigate the joint-targeting ability of CPPF, we performed in vivo fluorescence imaging at 6, 12, 24, and 48 h after intravenous injection of free Por, CPP, and CPPF into CIA mice (Figure 7A). Free Por showed rapid systemic distribution and clearance, with no obvious joint accumulation. CPP exhibited moderate joint retention, but the fluorescence signal was weak and diffused, and most of the fluorescence was concentrated in the liver and spleen due to non-specific uptake by the RES. In contrast, CPPF showed significant and sustained accumulation at the inflamed hind paws as early as 6 h post-injection, with the fluorescence intensity reaching a maximum at 24 h and remaining clearly visible at 48 h. This joint-targeting capability of CPPF compared to CPP can be attributed to the modification of FA-PEG-SH, which confers two synergistic advantages. First, the hydrophilic PEG chain provides a strong steric hindrance effect that effectively reduces non-specific protein adsorption and RES phagocytosis, thereby prolonging the blood circulation half-life of the nanoplatform. Second, the FA ligand mediates active targeting by specifically binding to folate receptors, which are highly overexpressed on activated macrophages in arthritic joints but minimally expressed on most normal tissues. Ex vivo fluorescence imaging of major organs and hind paws harvested at 48 h post-injection also confirmed this differential distribution pattern (Figure 7B).

Based on the optimal accumulation time determined by in vivo imaging, we evaluated

the in vivo photothermal performance of CPPF at 24 h post-injection. The inflamed hind paws of CIA mice were irradiated with an 808 nm laser for 5 min, and real-time thermal imaging was recorded (Figures 7C, 7D). The paw temperature increased rapidly and reached ~44 °C within 5 min, which is the optimal temperature range for mild PTT that can effectively induce immunomodulation without causing non-specific thermal damage to surrounding normal tissues.

Encouraged by the targeting and PTT performance, the long-term therapeutic potential of the sequential "apoptosis induction-immunomodulation" strategy was evaluated over a 21-day treatment cycle. For mice receiving laser irradiation, this dosing regimen was rationally designed to maximize M1 macrophage apoptosis while avoiding excessive PDT damage: specifically, PDT was administered once every 3 days, whereas mild PTT was performed daily. 660 nm PDT was performed once at 24 hours after each intravenous injection (given every 3 days) with a 3-min exposure to the hind paws. Concurrently, 808 nm mild PTT was delivered daily to the hind paws for 15 minutes over the entire treatment course. As shown in Figures 7E and 7F, saline-treated CIA mice developed severe arthritis, characterized by progressive paw swelling and increasing arthritis scores. Treatment with CPPF alone or PDT monotherapy partially alleviated the symptoms, evidenced by attenuated paw swelling and moderated arthritis scores compared to the saline group. However, the sequential therapy group exhibited the most significant therapeutic effect, demonstrating a sustained suppression of joint inflammation. Importantly, no significant body weight loss was observed in any of the treatment groups (Figure 7G), indicating that all therapeutic regimens were well-tolerated and did not cause obvious systemic toxicity. At the end of the treatment period, saline-treated mice showed severe paw redness and swelling, accompanied by high local temperature (Figure 7H). In contrast, the sequential therapy group showed markedly improved paw appearance, no obvious swelling, deformity, or increased local temperature. Micro-CT imaging revealed bone erosion and joint destruction in the saline group, while the sequential therapy group showed markedly attenuated bone damage. Quantitative analysis further confirmed these observations (Figure S16): the

bone volume/total volume (BV/TV) and trabecular number (Tb.N) were significantly increased, while trabecular separation (Tb.Sp) was significantly decreased in the sequential therapy group compared to the saline group, indicating effective inhibition of bone destruction and preservation of bone mass. In addition, we measured the concentrations of key inflammatory cytokines in joint tissue homogenates (Figure S17). Saline-treated CIA mice showed significantly elevated levels of pro-inflammatory cytokines TNF-α, IL-1β, and IL-6, accompanied by low levels of anti-inflammatory cytokines IL-10 and TGF-β. In contrast, the sequential therapy group showed significant reduction in pro-inflammatory cytokines and the highest levels of anti-inflammatory cytokines.

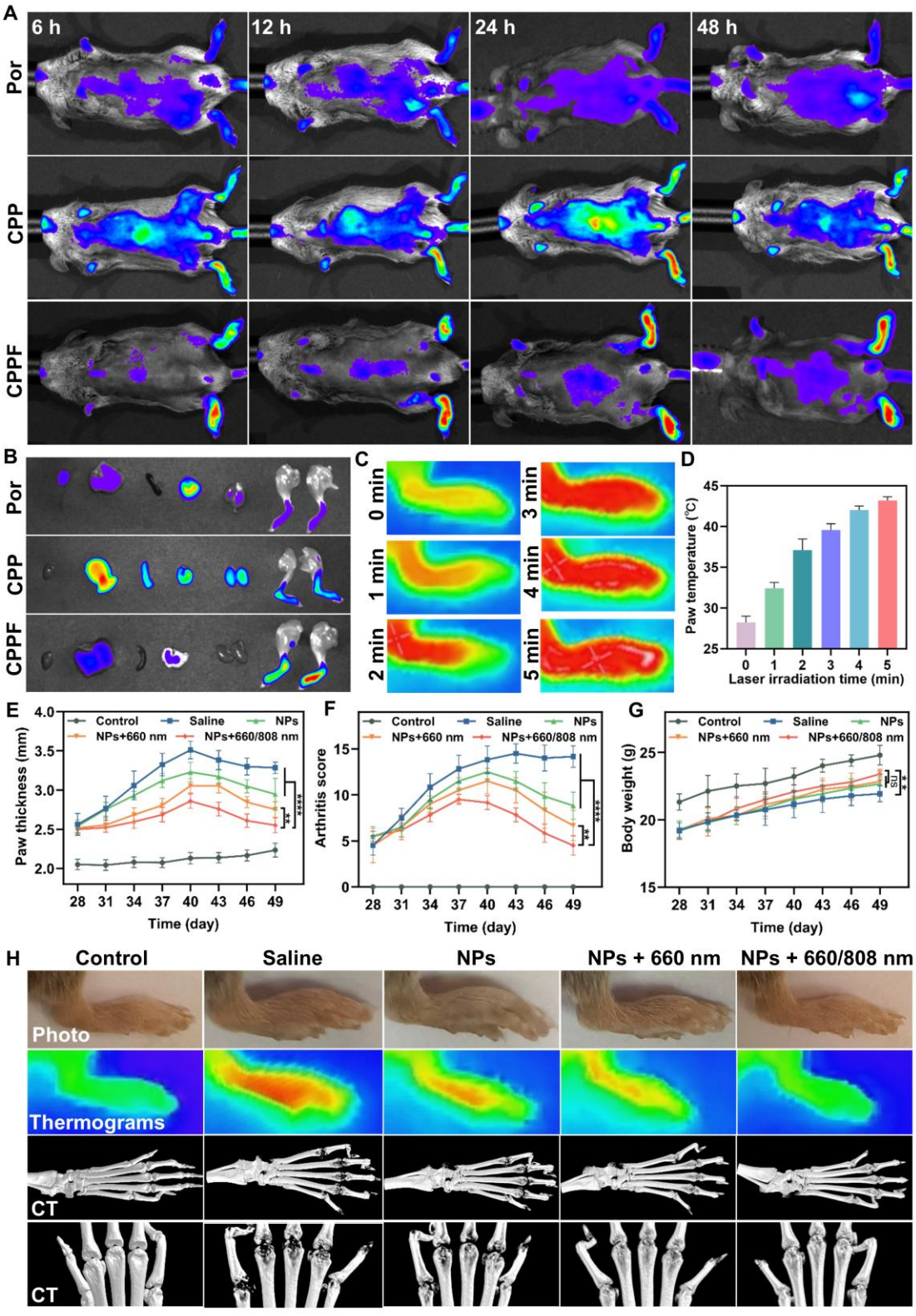


Figure 7. In vivo targeting, photothermal performance and therapeutic efficacy. (A) In vivo fluorescence images of CIA mice at 6, 12, 24, and 48 h after intravenous injection. (B) Ex vivo fluorescence images of major organs and hind paws from CIA mice at 48

h post-injection. (C) Infrared thermal images and (D) quantitative analysis of hind paws under 808 nm laser irradiation. (E) Changes in paw thickness, (F) arthritis scores, and (G) body weight of CIA mice in different treatment groups. (H) Photographs, infrared thermograms, and Micro-CT of hind paws from CIA mice in different treatment groups at the end of treatment. Statistical significance between groups was determined using one-way ANOVA, where * $p < 0.05$, ** $p < 0.01$, *** $p < 0.001$, and **** $p < 0.0001$.

These anti-inflammatory effects were further corroborated by histological analysis of joint tissues, which provided morphological evidence of the therapeutic efficacy (Figure 8). Hematoxylin and eosin (H&E) staining revealed massive inflammatory cell infiltration, synovial hyperplasia, and invasive pannus formation in the saline-treated group, which are hallmark pathological features of RA. Treatment with CPPF alone or PDT monotherapy moderately attenuated these pathological changes, but residual inflammatory infiltration and synovial thickening were still evident. In contrast, the sequential therapy group showed minimal inflammatory cell infiltration, and the least pannus formation. Safranin O-Fast Green (SO&FG) and Toluidine Blue (T&B) staining further confirmed the cartilage protective effect. Immunohistochemical and immunofluorescence staining provided molecular-level validation of the in vivo therapeutic mechanisms. Consistent with our in vitro experiments, the sequential therapy group exhibited the most significant macrophage polarization reprogramming, with markedly downregulated expression of the M1 macrophage marker iNOS and concomitantly upregulated expression of the M2 macrophage marker CD206. This phenotypic shift was accompanied by a restoration of cartilage homeostasis: the expression of the major cartilage matrix protein type II collagen (Col II) was increased, while the expression of the key cartilage-degrading enzyme MMP13 was suppressed. Notably, the sequential therapy group also showed significantly elevated expression of HSP70, a molecular chaperone that has been shown to exert anti-inflammatory and chondroprotective effects by inhibiting NF-κB signaling and promoting cartilage matrix synthesis [20, 53, 54].

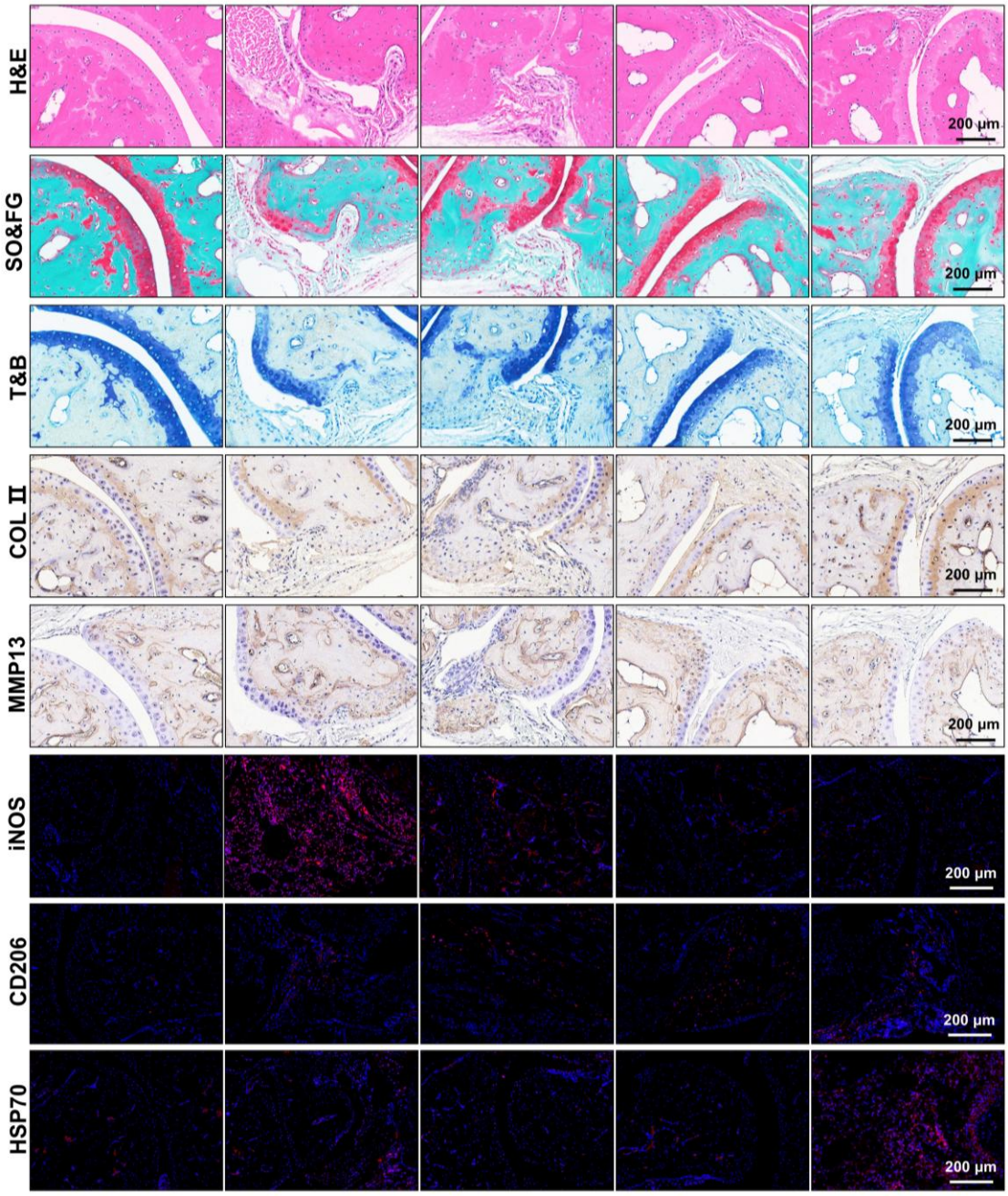


Figure 8. Histological and immunohistochemical analysis of hind paws from CIA mice after different treatments. H&E, SO&FG, T&B staining, immunohistochemistry staining of COL II and MMP13, and immunofluorescence staining of iNOS, CD206, and HSP70 in hind paw sections from different treatment groups.

Having demonstrated the therapeutic efficacy of CPPF-mediated sequential therapy, we also evaluated in vivo biosafety. At the end of the treatment period, histological analysis of major organs (heart, liver, spleen, lung, kidney) revealed no obvious pathological changes, inflammatory infiltration, or tissue damage in the sequential therapy group

compared to the healthy control group (Figure S18). Additionally, no significant abnormalities were observed in routine blood tests (Table S2). These results confirm that CPPF NPs exhibit excellent biocompatibility and does not cause significant systemic toxicity at the therapeutic dose used in this study.

Conclusion

In this study, we developed a targeted copper-based nanozyme platform (CPPF) for sequential phototherapy-enzymatic therapy of RA. The stepwise surface engineering strategy simultaneously resolved the poor aqueous solubility and non-specific distribution limitations of unmodified copper-based nanozymes, while retaining their robust SOD/CAT cascade activities. Benefiting from FA-mediated active targeting, CPPF NPs selectively accumulated in inflamed joints and implemented the "clearance first, remodeling later" therapeutic logic: rapid M1 macrophage apoptosis via 660 nm PDT, followed by 808 nm mild PTT synergizing with nanozyme activity to scavenge residual ROS, upregulate HSP70 and drive M2 polarization. Transcriptomic analysis confirmed the inhibition of TNF/NF-κB signaling and activation of Nrf2 antioxidant pathway. In CIA mice, CPPF NPs effectively alleviated synovial inflammation, prevented cartilage and bone destruction with excellent biosafety, providing a promising paradigm for macrophage-driven inflammatory disease treatment.

Declarations

Ethics approval statement

All animal experiments were approved by the Institutional Animal Care and Use Committee of Shanghai Ninth People's Hospital (No. SH9H-2026-A1299-1) and following National Institutes of Health guidelines.

Consent for publication

All the authors have agreed to publish this manuscript.

Data availability

The data are available from the corresponding author on reasonable request.

Competing interests

The authors declare no competing interest.

Funding

This work was financially supported by the National Natural Science Foundation of China (Grant No. 82370979, and 82301108).

Author contributions

Zeyu Han: Conceptualization, Methodology, Software, Data curation, Investigation, Writing-original draft, Formal analysis. Zhan Liu: Methodology, Software, Formal analysis, Investigation, Writing-original draft. Shoufu Sun: Conceptualization, Writing-original draft, Software, Methodology, Validation. Rui Chao: Methodology, Software, Formal analysis, Data curation. Xinao Fan: Methodology, Data curation, Software. Xuzhuo Chen: Writing-review & editing, Investigation, Methodology, Validation, Supervision. Fan Li: Supervision, Writing-original draft, Visualization, Writing-review & editing, Investigation. Shanyong Zhang: Funding acquisition, Writing-review & editing, Project administration, Visualization, Supervision.

References:

[1] A. Finckh, B. Gilbert, B. Hodkinson, S.-C. Bae, R. Thomas, K.D. Deane, D. Alpizar-Rodriguez, K. Lauper, Global epidemiology of rheumatoid arthritis, Nature Reviews Rheumatology 18 (10) (2022) 591-602.

[2] M. Rauner, A. Bozec, Mechanisms of osteoclast activation in inflammatory bone loss in rheumatoid arthritis, Nature Reviews Rheumatology 22 (1) (2026) 42-61.

[3] A. Shen, X. Cheng, Y. Cao, H.J.M.T.B. Deng, Multifunctional nanotherapeutics reprogramming the immunopathological landscape for rheumatoid arthritis therapy, Materials Today Bio (2025) 102379.

[4] M.C. Bruno, M.C. Cristiano, C. Celia, N. D'avanzo, A. Mancuso, D. Paolino, J. Wolfram, M.J.a.N. Fresta, Injectable drug delivery systems for osteoarthritis and rheumatoid arthritis, ACS Nano 16 (12) (2022) 19665-19690.

[5] J. Gan, D. Huang, J. Che, Y. Zhao, L. Sun, Biomimetic nanoparticles with cell-membrane camouflage for rheumatoid arthritis, Matter 7 (3) (2024) 794-825.

[6] M.M. Hanlon, C.M. Smith, M. Canavan, N.G. Neto, Q. Song, M.J. Lewis, A.M. O'rourke, O. Tynan, B.E. Barker, P.J.S.A. Gallagher, Loss of synovial tissue macrophage homeostasis precedes rheumatoid arthritis clinical onset, Science advances 10 (39) (2024) eadj1252.

[7] H. Huang, Y. Takakubo, Y. Takeda, T. Uno, H. Satake, H. Asao, M. Futakuchi, Y.P. Yang, S.B.

Goodman, M.J.A. Takagi, Increased macrophage autophagy with unique polarization in rheumatoid synovium, Autophagy (2026) 1-21.

[8] M.-W. Ma, K.-L. He, S. Zhou, Y.-G. Hu, K. Cheng, J.-X. Fan, B. Liu, L.-L. Dong, Y.-D. Zhao, Dual-Pronged Attack: Biomimetic Multi-Functional MOFs for Rheumatoid Arthritis Therapy via Inhibiting Synovial Hyperplasia and Improving Immune Microenvironment, ACS Nano 19 (29) (2025) 26525-26541.

[9] Y. Li, L. Cong, W. Zhang, R. Zhang, Y. Gao, S. Zheng, D. Li, Z. Zhang, L. Zhang, M.J.a.H.M. Yang, Macrophage Membrane-Coated Carbon Nanozymes for Targeted Drug Delivery and NIR-Responsive Synergistic Therapy in Rheumatoid Arthritis, Advanced healthcare materials 15 (6) (2026) e03316.

[10] Q. Liu, Y. Chen, X. Zhuang, J. Liu, H. Chen, Z. Shi, X. Li, Y. Li, Q. Luo, H.J.S. Wu, Betulinic Acid Self-Assembled Nanodelivery System Attenuates Osteoarthritis by Dually Modulating Macrophage Polarization and Macrophage-Chondrocyte Crosstalk via Disruption of the GSK3β/NF-κB/CCL20 Axis, Small 21 (50) (2025) e09306.

[11] X. Li, S. Li, X. Fu, Y.J.B.M. Wang, Apoptotic extracellular vesicles restore homeostasis of the articular microenvironment for the treatment of rheumatoid arthritis, Bioactive materials 35 (2024) 564-576.

[12] D. Guo, H. Liu, S. Zhao, X. Lu, H. Wan, Y. Zhao, X. Liang, A. Zhang, M. Wu, Z.J.B.M. Xiao, Synergistic rheumatoid arthritis therapy by interrupting the detrimental feedback loop to orchestrate hypoxia M1 macrophage polarization using an enzyme-catalyzed nanoplatform, Bioactive materials 41 (2024) 221-238.

[13] H. Zhang, J. Jia, H. Liu, H. Han, Q.J.N.C. Li, Near-infrared light-driven metabolic reprogramming of synoviocytes for the treatment of rheumatoid arthritis, Nature communications 16 (1) (2025) 6590.

[14] S. Xiao, S. Huang, M. Wang, T. Wang, M. Han, Y. Deng, W. Geng, L. Cheng, X. Wang, L.J.a.M. Ma, Biocatalytic and Redox-Regulated Nanoarchitectures for Precision Inflammation and Immune Homeostasis Modulation to Combat Rheumatoid Arthritis, Advanced materials 37 (33) (2025) 2502147.

[15] N. Jia, Y. Gao, M. Li, Y. Liang, Y. Li, Y. Lin, S. Huang, Q. Lin, X. Sun, Q.J.S.T. He, T. Therapy, Metabolic reprogramming of proinflammatory macrophages by target delivered roburic acid effectively ameliorates rheumatoid arthritis symptoms, Signal transduction and targeted therapy 8 (1) (2023) 280.

[16] Z. Li, B. Wu, W. Li, E. Marsili, K. Tang, K. Sun, Z. Cao, Y. Zhang, H. Huang, X. Li, G. Wang, Unlocking an Efficient SOD-to-CAT Catalytic Relay in a MOF Nanozyme via Dopamine-Driven Interfacial Nanoreconstruction for Osteoarthritis Therapy, Advanced Materials 38 (19) (2026) e72747.

[17] S. Zhou, Y. Li, Y.-T. Zhou, M.-W. Ma, K.-L. He, K. Cheng, J.-X. Fan, B. Liu, L.-L. Dong, Y.-D. Zhao, X. Liu, An enhanced nanoenzyme for remodeling the inflammatory microenvironment and low-temperature photothermal cascade therapy for rheumatoid arthritis, Chemical Engineering Journal 525 (2025) 169877.

[18] S. Priya, D. Sharma, K.K. Jain, S. Chutani, G.J.N.A. Singhvi, Targeted nanocarriers integrating photodynamic and photothermal therapy: a paradigm shift in rheumatoid arthritis treatment, Nanoscale Advances 8 (3) (2026) 725-742.

[19] L. Mi, J. Gao, Y. Liu, N. Zhang, M. Zhao, S. Wang, K.J.R. Xu, Autoimmunity, Photodynamic

therapy for arthritis: A promising therapeutic strategy, Rheumatology & Autoimmunity 3 (04) (2023) 205-219.

[20] G. Xue, H. Jiang, Z. Song, Y. Zhao, W. Gao, B. Lv, J.J.a.S. Cao, Dual Targeting Biomimetic Carrier-Free Nanosystems for Photo-Chemotherapy of Rheumatoid Arthritis via Macrophage Apoptosis and Re-Polarization, Advanced science 12 (10) (2025) 2406877.

[21] Y. Wu, Y. Ge, Z. Wang, Y. Zhu, T. Tian, J. Wei, Y. Jin, Y. Zhao, Q. Jia, J.J.J.O.N. Wu, Synovium microenvironment-responsive injectable hydrogel inducing modulation of macrophages and elimination of synovial fibroblasts for enhanced treatment of rheumatoid arthritis, Journal of nanobiotechnology 22 (1) (2024) 188.

[22] Z. Li, Y. Yang, Y. Shi, D. Hu, D. Gao, Y. Zhang, H. Yu, Z. Luo, Q. Saiding, N.J.N.N. Kong, Bioengineered photosynthetic nanothylakoids reshape the inflammatory microenvironment for rheumatoid arthritis therapy, Nature nanotechnology 21 (1) (2026) 125-139.

[23] Y. Li, J. Hu, B. Ran, H. Zhong, N. Zhong, Y. Zhong, X. Fu, X. Liu, G. Wu, Q.J.M.T.B. Zhong, Dual-responsive PDA-HP hydrogel enables mitochondria-targeted mild photothermal therapy for spinal cord repair, Materials Today Bio (2026) 102783.

[24] M. Wu, D. Xie, L. Wang, Z. Liu, H. Bao, T. Ye, C. Hong, J. Lin, T. Chen, A. Wu, Q. Li, Spatiotemporally targeted nanocapsules combined with mild photothermal therapy regulate the synovial microenvironment in rheumatoid arthritis, Bioactive Materials 58 (2026) 33-48.

[25] B. Li, F. Liu, J. Ye, X. Cai, R. Qian, K. Zhang, Y. Zheng, S. Wu, Y. Han, Regulation of Macrophage Polarization Through Periodic Photo-Thermal Treatment to Facilitate Osteogenesis, Small 18 (38) (2022) 2202691.

[26] Y. Zhu, H. Liu, P. Wu, Y. Chen, Z. Deng, L. Cai, M.J.T. Wu, Multifunctional injectable hydrogel system as a mild photothermal-assisted therapeutic platform for programmed regulation of inflammation and osteo-microenvironment for enhanced healing of diabetic bone defects in situ, Theranostics 14 (18) (2024) 7140.

[27] S. Ren, Y. Xu, X. Dong, Q. Mu, X. Chen, Y. Yu, G.J.J.O.N. Su, Nanotechnology-empowered combination therapy for rheumatoid arthritis: principles, strategies, and challenges, Journal of nanobiotechnology 22 (1) (2024) 431.

[28] M. Zhang, R. Zhang, Y. Dong, J. Liu, Z. Gao, X. Zhou, J. Cao, Oxygen supplementation liposomes for rheumatoid arthritis treatment via synergistic phototherapy and repolarization of M1-to-M2 macrophages, Chemical Engineering Journal 459 (2023) 141484.

[29] S. Priya, D. Sharma, K.K. Jain, S. Chutani, G. Singhvi, Targeted nanocarriers integrating photodynamic and photothermal therapy: a paradigm shift in rheumatoid arthritis treatment, Nanoscale Advances 8 (3) (2026) 725-742.

[30] M. Wu, H. Li, P. Wang, T. He, M. Zhu, X. Qin, B. Zhang, M. Cui, B. Song, Y.J.S. He, Spatial Confinement-Engineered Heteronuclear Diatomic Nanozymes for Modulation of Immune Homeostasis in Rheumatoid Arthritis, Small (2026) e73633.

[31] Q. Miao, H. Yang, X. Zhu, X. Feng, J. Yang, Y.J.C.C.R. Wang, Cascade nanozymes as ROS scavengers for the treatment of aseptic inflammation, Coordination Chemistry Reviews 548 (2026) 217163.

[32] R. Chen, Y. Su, G. Zhao, J. Tao, Q. Diao, G. Xiang, T. Jiang, L. Han, X. Zhao, Nanozyme-Integrated Hydrogel Targeting AGEs for Diabetic Osteoarthritis Therapy, Advanced Science 13 (8) (2026) e16389.

[33] C.S. Lin, M.Q. He, M.Y. An, Q.H. Zhao, Z.H. Zhang, K.Y. Deng, Y. Ai, H.B.J.S. Xin, Ultra-

Small Copper-Based Multienzyme-Like Nanoparticles Protect Against Hepatic Ischemia-Reperfusion Injury Through Scavenging Reactive Oxygen Species in Mice, Small 20 (51) (2024) 2403313.

[34] X. Chen, Y. Du, Y. Huang, X. Zhou, X. Xie, C. Li, C. Zhao, F. Dai, X. Yu, S. Zhang, Ultrasmall copper-based clusterzymes ameliorate Achilles tendinopathy by inhibiting acute oxidative stress, Nano Research 17 (6) (2024) 5374-5389.

[35] C. Huang, Z. Liu, Y. Deng, X. Wang, Q. Miao, D. Sun, X. Zhu, J. Yang, Y.J.T. Wang, Ultrasmall radical metal organic cage as cascade antioxidant nanozyme for renal injury, Theranostics 15 (6) (2025) 2564.

[36] Z. Ma, M. Li, R. Guo, Y. Tian, Y. Zheng, B. Huang, Y. You, Q. Xu, M. Cui, L.J.S.A. Shen, Treating myocardial infarction via a nano-ultrasonic contrast agent-mediated high-efficiency drug delivery system targeting macrophages, science advances 11 (1) (2025) eadp7126.

[37] Z. Han, Y. Li, X. Zhan, M. Sun, Y. Liang, M. Yuan, Y. Sun, J. Cao, B. Zhao, F.J.T. Li, A versatile nanoplatform with excellent biofilm permeability and spatiotemporal ROS regulation for peri-implantitis treatment, Theranostics 15 (8) (2025) 3490.

[38] A. Olejnik, M. Ficek, M. Szkodo, A. Stanisławska, J. Karczewski, J. Ryl, A. DołęGa, K. Siuzdak, R.J.a.N. Bogdanowicz, Tailoring diffusional fields in zwitterion/dopamine copolymer electropolymerized at carbon nanowalls for sensitive recognition of neurotransmitters, ACS Nano 16 (8) (2022) 13183-13198.

[39] J. Yu, T. Marchesi D'alvise, I. Harley, A. Krysztofik, I. Lieberwirth, P. Pula, P.W. Majewski, B. Graczykowski, J. Hunger, K.J.a.M. Landfester, Ion and molecular sieving with ultrathin polydopamine nanomembranes, Advanced materials 36 (29) (2024) 2401137.

[40] A. Abdul Rahman, I.L. Mohd Isa, M.J. Biggs, A.J.a.a.M. Pandit, Interfaces, Diatom-Based Artificial Antigen-Presenting Cells: A Novel Approach for Adaptive Immune Modulation, ACS applied materials & interfaces 17 (26) (2025) 37718-37734.

[41] Z. Han, Y. Liang, Y. Li, M. Yuan, X. Zhan, J. Yan, Y. Sun, K. Luo, B. Zhao, F. Li, Programmed Cascade Polydopamine Nanoclusters for Pyroptosis-Based Tumor Immunotherapy, Small 20 (42) (2024) 2401397.

[42] Z. Li, X. Shan, Z. Chen, N. Gao, W. Zeng, X. Zeng, L.J.a.S. Mei, Applications of surface modification technologies in nanomedicine for deep tumor penetration, Advanced science 8 (1) (2021) 2002589.

[43] H. Weng, W. Zou, F. Tian, H. Xie, A. Liu, W. Liu, Y. Liu, N. Zhou, X. Cai, J.J.N.C. Wu, Inhalable cardiac targeting peptide modified nanomedicine prevents pressure overload heart failure in male mice, Nature communications 15 (1) (2024) 6058.

[44] D. Peng, S. Huang, M. Que, X. Deng, Z. Zhou, H.J.C.S. Qiu, Copper-based single-atom nanozymes: from fundamental insights to biomedical applications, Chemical science (2026)

[45] A. Carmignani, T. Yamazaki, M. Battaglini, C.Q. Vu, A. Marino, S. Takayanagi-Kiya, T. Kiya, A. Armirotti, A. Di Fonzo, S.J.a.N. Arai, Cellular activity modulation mediated by near infrared-irradiated polydopamine nanoparticles: in vitro and Ex Vivo investigation, ACS Nano 19 (17) (2025) 16267-16286.

[46] Q. Qin, Y. Zhou, P. Li, Y. Liu, R. Deng, R. Tang, N. Wu, L. Wan, M. Ye, H.J.J.O.N. Zhou, Phase-transition nanodroplets with immunomodulatory capabilities for potentiating mild magnetic hyperthermia to inhibit tumour proliferation and metastasis, Journal of nanobiotechnology 21 (1) (2023) 131.

[47] H. Zhao, W. Shao, M. Jiang, F. Chen, Y. Li, X. Zhang, T. Ma, M. Chen, B. Sun, Z.J.T. Wang, Spatiotemporal NO/O2-releasing cascade nanozyme microneedles enhance diabetic infected wound healing by modulating the immune microenvironment, Theranostics 16 (6) (2026) 2811.

[48] P. Yu, Y. Li, H. Sun, H. Zhang, H. Kang, P. Wang, Q. Xin, C. Ding, J. Xie, J. Li, Mimicking Antioxidases and Hyaluronan Synthase: A Zwitterionic Nanozyme for Photothermal Therapy of Osteoarthritis, Advanced Materials 35 (44) (2023) 2303299.

[49] M.S. Kalairaj, R. Pradhan, W. Saleem, M.M. Smith, A.K.J.a.H.M. Gaharwar, Intra-articular injectable biomaterials for cartilage repair and regeneration, Advanced healthcare materials 13 (17) (2024) 2303794.

[50] W. Liu, N.Y. Guo, J.Q. Wang, B.B.J.M. Xu, Osteoarthritis: mechanisms and therapeutic advances, MedComm 6 (8) (2025) e70290.

[51] S. Koo, H.S. Sohn, T.H. Kim, S. Yang, S.Y. Jang, S. Ye, B. Choi, S.H. Kim, K.S. Park, H.M.J.N.N. Shin, Ceria-vesicle nanohybrid therapeutic for modulation of innate and adaptive immunity in a collagen-induced arthritis model, Nature nanotechnology 18 (12) (2023) 1502-1514.

[52] Y. Zhang, X. Kang, J. Li, J. Song, X. Li, W. Li, J. Qi, Inflammation-Responsive Nanoagents for Activatable Photoacoustic Molecular Imaging and Tandem Therapies in Rheumatoid Arthritis, ACS Nano 18 (3) (2024) 2231-2249.

[53] A. Liu, Q. Wang, Z. Zhao, R. Wu, M. Wang, J. Li, K. Sun, Z. Sun, Z. Lv, J.J.a.N. Xu, Nitric oxide nanomotor driving exosomes-loaded microneedles for achilles tendinopathy healing, ACS Nano 15 (8) (2021) 13339-13350.

[54] Y. Guo, T. Stampoultzis, P. Karami, N. Nasrollahzadeh, V.K. Rana, D.P.J.O. Pioletti, Cartilage, HSP70—A key regulator in chondrocyte homeostasis under naturally coupled hydrostatic pressure-thermal stimuli, Osteoarthritis and cartilage 32 (8) (2024) 896-908.

Supplementary Files

This is a list of supplementary files associated with this preprint. Click to download.

- SupportingInformation.docx